

Supporting Information

**Breaking the Brønsted-Evans-Polanyi Relation in N₂ Adsorption
Driven by Potential-Dependent Repositioning of Frontier
Orbitals: A Sweet Marriage of Machine Learning-Assisted
Screening and Electric Double-Layer Effect**

Yali Lu^a, Ning Guo^b, Qiang Zhang^{*a}, Zongjin Hu^a, Chenglong Shi^a, Weiju Hao^b, Yuling
Song^c, Qingjun Zhou^a, Jianglong Mu^a

a. Department of Physics, University of Shanghai for Science and Technology, Shanghai 200093,

People's Republic of China

b. School of Materials and Chemistry, University of Shanghai for Science and Technology, Shanghai

200093, People's Republic of China

c. College of Physics and Electronic Engineering, Nanyang Normal University, Nanyang 473061,

People's Republic of China

* Corresponding author.

*Address correspondence to E-mail: qiangzhang@usst.edu.cn

S1. Computational details.

Note S1. Calculation of adsorption energy.

The energy released or absorbed by different intermediates as they adsorb to surfaces or other molecules during the NRR process.

$$E_{\text{ads}} = E_{\text{total}} - E_{\text{adsorbate}} - E_{\text{g-C}_{16}\text{N}_5} \quad (\text{S1})$$

where E_{total} , $E_{\text{adsorbate}}$, and $E_{\text{g-C}_{16}\text{N}_5}$ are the total energy of the adsorbed intermediates on the TM@g-C₁₆N₅, the isolated adsorbate, and the g-C₁₆N₅, respectively. According to this definition, a smaller (or more negative) value of E_{ads} indicates a stronger adsorption energy of the intermediate on the catalyst or substrate surface, which means that the adsorption is more stable and tightly bound.

Note S2. Calculation of Gibbs free energy.

The Computational Hydrogen electrode (CHE) model, based on Nørskov and his team ¹, is used to calculate the change in free energy (ΔG) in each of the key steps of the NRR:

$$\Delta G = \Delta E + \Delta E_{\text{ZPE}} - T\Delta S + \Delta G_{\text{U}} + \Delta G_{\text{pH}} \quad (\text{S2})$$

where ΔE represents the change of reaction energy, ΔE_{ZPE} represents the change of zero-point energy, and ΔS represents the change of entropy. T stands for the temperature of 298.15 K. Zero-point energy and entropy can be obtained from vibration frequency calculations, where data for gas phase frequency molecules come from the National Institute of Standards and Technology (NIST) database. ΔG_{U} represents the effect of applied electrode potential. The concentration sum of H^+ contribution to ΔG_{pH} can be calculated by the following formula:

$$\Delta G_{\text{pH}} = 2.303 \times \kappa_{\text{B}} T \times \text{pH} \quad (\text{S3})$$

where κ_{B} is the Boltzmann constant and pH is set to zero to simulate acidic conditions.

The catalytic performance was evaluated by theoretical limit potential (U_{L})

$$U_{\text{L}} = \left(\frac{-\Delta G_{\text{max}}}{e} \right) \quad (\text{S4})$$

where ΔG_{max} represents the highest positive ΔG of the potential-determining step in the six-electron step of NRR.

Note S3. Calculation of ΔE_b and E_{form} .

Consequently, the stability was systematically evaluated according to the following

formulas:

$$E_{\text{bind}} = E_{\text{TM@g-C}_{16}\text{N}_5} - E_{\text{g-C}_{16}\text{N}_5} - E_{\text{TM}}^{\text{DFT}} \quad (\text{S5})$$

$$E_{\text{form}} = E_{\text{TM@g-C}_{16}\text{N}_5} - E_{\text{g-C}_{16}\text{N}_5} - E_{\text{TM}}^{\text{exp}} \quad (\text{S6})$$

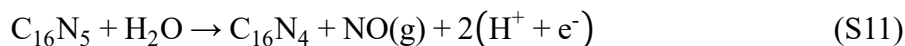
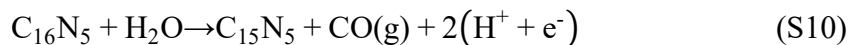
$$E_{\text{coh}} = (E_{\text{TM-bulk}} - nE_{\text{TM}}^{\text{DFT}})/n = E_{\text{TM}}^{\text{exp}} - E_{\text{TM}}^{\text{DFT}} \quad (\text{S7})$$

$$\Delta E_b = E_{\text{bind}} - E_{\text{coh}} \quad (\text{S8})$$

where $E_{\text{TM@g-C}_{16}\text{N}_5}$, $E_{\text{g-C}_{16}\text{N}_5}$, $E_{\text{TM}}^{\text{DFT}}$, and $E_{\text{TM-bulk}}$ denote the energies of TM@g-C₁₆N₅, g-C₁₆N₅, single TM, and the TM bulk, respectively; n represents the number of TM atoms, and E_{coh} refers to the cohesive energy of the TM atoms.

Note S4. Electrochemical durability of TM@g-C₁₆N₅.

Carbon/nitrogen-based catalysts employed in nitrogen reduction reactions (NRR) commonly experience electrochemical decomposition phenomena that involve reduction and oxidation reactions. Specifically, these reactions entail $\text{N} + 3\text{H}^+ + 3\text{e}^- \rightarrow \text{NH}_3(\text{g})$, $\text{C} + \text{H}_2\text{O} \rightarrow \text{CO}(\text{g}) + 2\text{H}^+ + 2\text{e}^-$, and $\text{N} + \text{H}_2\text{O} \rightarrow \text{NO}(\text{g}) + 2\text{H}^+ + 2\text{e}^-$. We use thermodynamic calculation methods to evaluate the likelihood of substrate decomposition² to determine the potential of carbon/nitrogen-based catalysts to suffer degradation under electrochemical conditions. This approach provides a more detailed and academic approach. According to Fig. S21, we observed that g-C₁₆N₅ was degraded into ammonia (NH₃), carbon monoxide (CO), and nitrogen oxides (NO). The degradation process of g-C₁₆N₅ can be described as follows:



the potential U_d was required to drive the decomposition to release CO/NO by

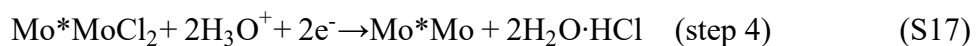
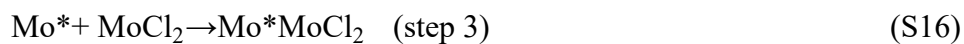
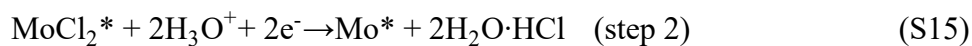
$$U_d = \Delta G_d / 2e \quad (\text{S12})$$

while that to release NH₃ can be obtained by

$$U_d = \Delta G_d / 3e \quad (\text{S13})$$

Note S5. Synthetic feasibility of Mo@g-C₁₆N₅ in experiment.

For the synthesis of single-atom catalysts (SACs), wet chemistry method is a very promising way to achieve highly dispersed single atoms³. Based on previous research⁴, we selected MoCl₂ as the metal precursor and evaluated the feasibility of preparing Mo@g-C₁₆N₅ using first-principles calculations. We calculated in detail the energy changes along the proposed pathway (see Fig. S21). The specific reaction steps are as follows:



where * is g-C₁₆N₅.

Note S6. Calculations for the GBR model.

The best performing Gradient Boosted Regression (GBR) model is an integrated machine learning algorithm that is generated by integrating multiple weak regression trees^{5,6}. Given a set of training samples $D = \{(x_1, y_1), (x_2, y_2), \dots, (x_n, y_n)\}$ where the number of leaf nodes in each regression tree is J . We partition the input data into J disjoint regions and define each regression tree as $t_m(x)$. The training objective of the GBR is to minimize a loss function L , and empirically minimize the risk by determining the parameters of the decision tree θ_m .

$$\theta_m = \underset{\theta_m}{\operatorname{argmin}} \sum_{i=1}^n L(y_i, f_{(m-1)}(x_i) + t_m(x_i)) \quad (\text{S18})$$

The GBR training procedure is as follows:

(a) Initialize the regression tree function $f_0(x)$.

(b) Train the GBR in the gradient descent direction and compute the negative gradient value of the loss function as an estimate of the residuals. At the m th iteration, the GBR generates a regression tree function to fit the residuals and updates the current function $f_m(x)$.

(c) The final regression model is a weighted sum of several weak regression trees, defined as follows:

$$f_M(x) = \sum_{m=1}^M t(x, \theta_m) \quad (\text{S19})$$

Note S7. Calculation of the RFR model.

Random Forest Regression (RFR) model is an integrated machine learning algorithm that generates powerful regression models by integrating multiple decision trees^{7,8}. Given a set of training samples $D = \{(x_1, y_1), (x_2, y_2), \dots, (x_n, y_n)\}$, each decision tree is constructed with randomly drawn subsamples from the training samples and trained on these subsamples.

The training objective of RFR is to improve the generalization ability of the model by reducing the prediction error. The specific computational process is as follows:

(a) Initialization: Define the number N of trees to be constructed.

(b) Constructing trees:

1. For the k th tree, randomly draw a subsample set D_k with put-back from the training sample set.

2. Use the subsample set D_k to construct the decision tree T_k . The split selection for each node selects the best split from a random subset of features to increase the diversity of the model.

(c) Integrated prediction: the predictions from all trees are averaged to obtain the final regression prediction model $f(x)$:

$$f(x) = \frac{1}{N} \sum_{k=1}^N T_k(x) \quad (\text{S20})$$

Note S8. Calculation of SVR model.

Support Vector Regression (SVR) is a regression analysis algorithm based on Support Vector Machine (SVM). Given a set of training samples $D = \{(x_1, y_1), (x_2, y_2), \dots, (x_n, y_n)\}$, SVR aims to find a regression function $f(x) = w \cdot x + b$ that keeps most of the data points within the error ϵ while keeping the model simple ⁹.

The goal of SVR is to minimize the following equation:

$$\min_{w,b} \frac{1}{2} \|w\|^2 + c \sum_{i=1}^n \max(0, |y_i - (w \cdot x_i + b)| - \epsilon) \quad (\text{S21})$$

SVR training process: (a) Initialize parameters: choose the regularization parameter C and the error threshold ϵ .

(b) Construct the optimization problem: Convert the regression problem into a convex optimization problem by introducing relaxation variables.

(c) Solve the optimization problem: Use an algorithm (e.g., SMO algorithm) to solve for the optimal regression function parameters w and bias b .

(d) Construct the regression function: obtain the final regression model $f(x)$.

The final regression model for SVR is:

$$f(x) = \sum_{i=1}^n (\alpha_i - \alpha_i^*) K(x_i, x) + b \quad (\text{S22})$$

where α_i and α_i^* are the Lagrange multipliers of the support vectors, $K(x_i, x)$ is the kernel function, and b is the bias term. SVR obtains a regression model with good generalization ability by optimizing so that most of the data points are within ϵ and controlling the model complexity.

Note S9. Calculation of the ETR model.

Extreme Random Trees (ETR) is an integrated learning algorithm that performs regression prediction by constructing multiple completely randomized decision trees ¹⁰. Given a training sample set $D = \{(x_1, y_1), (x_2, y_2), \dots, (x_n, y_n)\}$, ETR splits the nodes by randomly selecting features and thresholds.

ETR training process: (a) Initialization: define the number N of trees to be constructed.

(b) Construct each tree: 1. For the k th tree, randomly select a subsample set D_k from the training sample set. 2.

2. At each node, randomly select a feature and a threshold for splitting.

3. Repeat the process until a preset tree depth is reached or the number of samples in a node is less than a preset value.

(c) Integrated prediction: average the prediction results from all trees to obtain the final regression prediction model $f(x)$.

$$f(x) = \frac{1}{N} \sum_{k=1}^N T_k(x) \quad (\text{S23})$$

where $T_k(x)$ is the prediction of the k th tree. the final regression model of ETR is obtained by averaging the predictions of all decision trees.

Note S10. Calculation of the SISSO model.

Sure Independence Screening and Sparsifying Operator (SISSO) is a sparse regression method that combines symbolic regression with compressed sensing for selecting physically interpretable and predictive features from high-dimensional feature space. Its core computational method consists of the following steps:

1. Feature space construction

First, a set of initial basic features (primary features) is defined, which represent the relevant attributes in the fields of physics, chemistry, and so on. Then, a series of symbolic operators (e.g., addition, multiplication, exponentiation, logarithm, etc.) are used to generate complex derived features to extend the feature space through multiple iterative operations. The generated feature space contains possible nonlinear combinations and is denoted as $F = \{f_1, f_2, \dots, f_N\}$ where N is the number of candidate features generated by mathematical operations¹¹.

2. Sure Independence Screening (SIS)

With such a large feature space, SIS is used to screen features by their correlation with the target variable. In this process, all features are ranked based on their Pearson correlation coefficients with the target variable and only the top M features that are most relevant to the target are retained to form a sparse feature subspace. This step significantly reduces the number of features while retaining the features that are most likely to influence the predictive models¹¹.

3. Sparsifying Operator (SO)

After filtering out the relevant features, SISSO further selects features through Sparsifying Operator (SO). Specifically, L0 regularized regression is used to solve the following optimization problem:

$$\min_{\beta} \|y - D\beta\|^2 + \lambda \|\beta\|_0 \quad (\text{S24})$$

where, y is the target attribute, D is the feature matrix, β is the linear regression coefficient, and λ is the regularization parameter to control sparsity¹¹. By determining the optimal combination of features and model dimensions through cross-validation, SISSO finally selects a sparse linear model that can predict the target attribute well and has high interpretability.

4. Model validation and optimization

Models are evaluated through cross-validation (e.g., leave-one-out or other methods) to ensure the generalization ability of the model on different datasets. In multidimensional regression or classification problems, SISSO can select the best dimensional characterizer based on the validation error. For classification tasks, SISSO constructs multi-hyperplane models to classify different classes by methods such as Support Vector Machines (SVMs)¹².

S2. Screening of highly stable and active NRR catalysts for TM@g-C₁₆N₅

To create single-atom catalysts with exceptional stability and activity, a selection of 27 TM atoms was anchored on a g-C₁₆N₅ substrate with a 2 × 2 × 1 supercell ($a = b = 12.22 \text{ \AA}$) (Fig. S1a) to investigate the structure-activity relationship. The sufficiently large hexagonal lattice of g-C₁₆N₅ ensures adequate spacing between the TM atoms, thereby minimizing interactions between periodically positioned TM atoms, as achieved in the TM@g-C₁₆N₅ configuration. Fig. S1b reveals that N₂ reduction can occur via two distinct adsorption models encompassing the distal, alternating, enzymatic, and consecutive pathways, with the NRR activity typically assessed by the limiting potential (U_L), the minimum required to initiate the NRR process. Given the intrinsic complexity of the NRR, the formulation of robust screening descriptors is paramount, prompting the development of a 'Five-Step' strategy, as detailed below (Fig. S1c): firstly, SACs should demonstrate high thermodynamic stability; secondly, effective N₂ activation must be achieved, signaled by a $\Delta G^*_{N_2}$ value below -0.10 eV; thirdly and fourthly, the $\Delta G^*_{N_2 \rightarrow N_2H}$ and $\Delta G^*_{NH_2 \rightarrow NH_3}$ values lower than 0.98 eV (consistent with Ru (0001))¹³; finally, the U_L of the NRR surpasses that of the competing HER by a minimum of -0.5 volts^{14, 15}.

In SACs, the propensity of dispersed metal atoms to form clusters, driven by the high surface energy of their supports, necessitates an evaluation of their stability and feasibility through the assessment of the energy difference (ΔE_b) and formation energy (E_{form}) (see Note S3), respectively. A negative ΔE_b indicates a thermodynamic preference for TM atoms to remain dispersed on the g-C₁₆N₅ substrate rather than forming clusters, whereas a positive ΔE_b implies that single TM atoms could achieve stability on the substrate if the aggregation barrier

is sufficiently high to inhibit clustering, thereby ensuring the kinetic stability of the SACs (Specific data in Table S1). However, it should be noted that the values of E_{form} and ΔE_{b} can be slightly larger than zero in practical applications, because the migration of TM atoms needs to overcome a high energy barrier¹⁶. Overall, Fig. S1d demonstrates that all 27 structures exhibit robust interatomic interactions that resist dissociation, demonstrating a clear energetic preference for dispersed deposition of TM atoms on g-C₁₆N₅ over clustering, thereby marking them as compelling subjects for future exploration. Meanwhile, the strong interaction between the TM atoms and the g-C₁₆N₅ framework, as demonstrated by Bader charge analysis, is crucial for preventing the aggregation of TM atoms. Consequently, to further elucidate the stability of TM@g-C₁₆N₅, we decomposed the matrix into three distinct components: the TM atoms, the N₄ unit bonded to the TM atoms, and the remaining g-C₁₆N₅ moiety, facilitating a comprehensive analysis of charge transfer among these parts. The Bader charge analysis (Fig. S2) indicates that each TM atom acquires a positive charge through electron transfer to the nitrogen atoms. The initial decrease in the number of electrons transferred with rising atomic number within each period can be attributed to the growing electron affinity in the TM-*d* orbitals, where the progressively fewer empty orbitals function as increasingly potent electron acceptors, whereas the subsequent decline in transferred charge for later TM atoms is due to the relatively high occupancy of their *d*-orbitals. The charge transfer scenarios presented in Figs. S3–S5 elucidate the interactions described above, wherein the resulting positively charged TM atoms emerge as crucial centers for adsorption and activation throughout the NRR process.

Three possible initial configurations for N₂ adsorption and activation on TM@g-C₁₆N₅,

as shown in Fig. S6, were considered, with the corresponding free energies of N₂ adsorption ($\Delta G^*_{N_2}$) compared in Fig. S1e and the associated TM-N bond lengths detailed in Table S2. As shown in Fig. S1e and Table S2, based on criteria 1 and 2, we selected 10 catalysts (TM = Ti, V, Nb, Mo, Ru, Hf, Ta, W, Re, and Os) for further investigation. Following criteria 3 and 4, Nb, Ru, Hf, Ta, W, Re and Os are excluded from consideration, as these materials are ineffective in catalyzing the conversion of N₂ into N₂H or NH₂ into NH₃ (Figs. S1f-h). As illustrated in Fig. S1i, although the PDS for Ti and Mo is located in the final stage of the deammoniation process and for V in the initial step of hydrogenation, all three catalysts meet the screening criteria and are viable candidates. Given that the HER is the primary competing side reaction during the NRR, we ultimately assess the NRR selectivity based on the difference in limiting potentials between NRR and HER ($U_{L(NRR)} - U_{L(HER)} > -0.5 \text{ V}$)^{14, 15}, only Mo@g-C₁₆N₅ met the screening criteria (Fig. S1j).

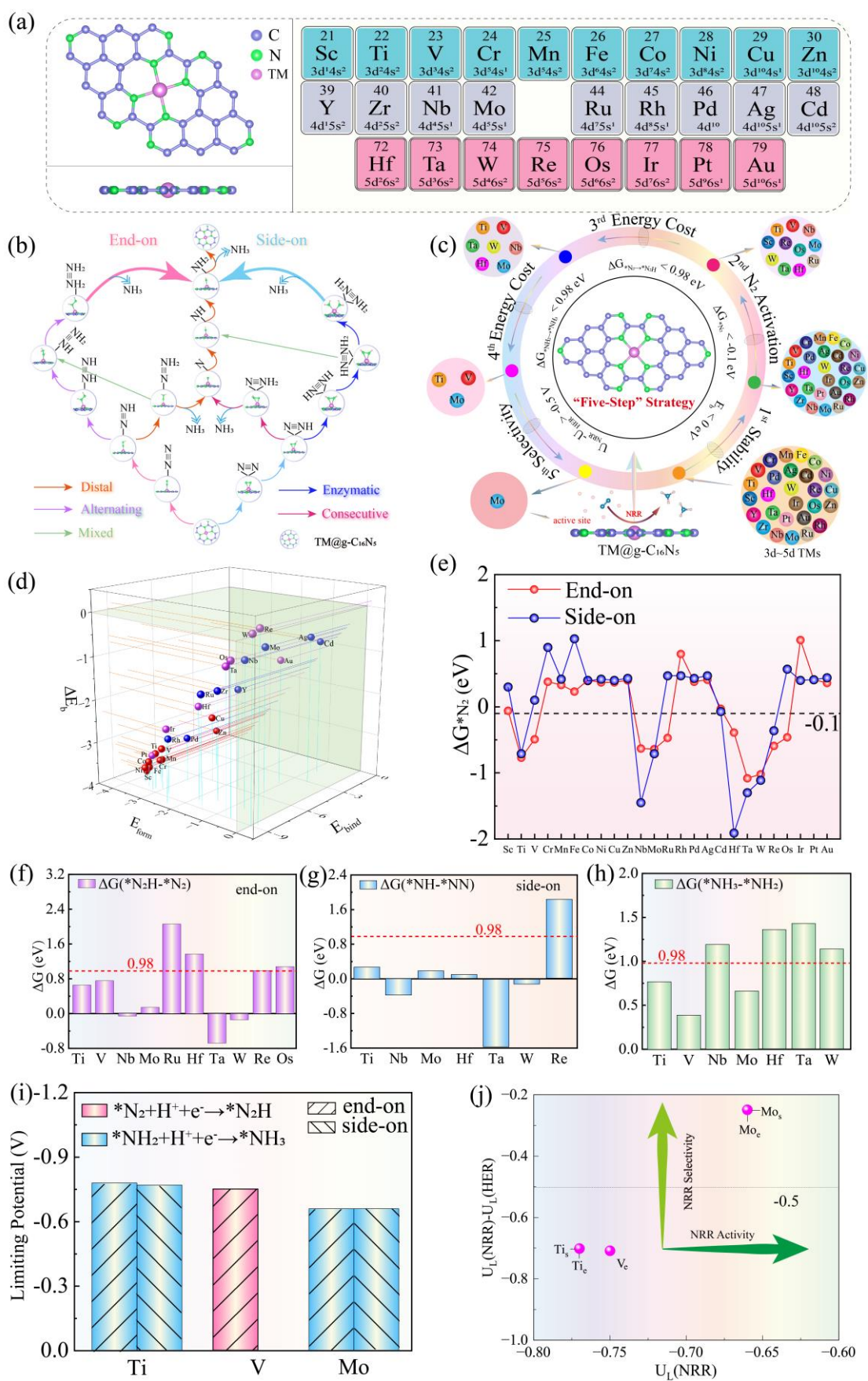


Fig. S1. (a) Structural arrangement of the transition metal (TM) embedded within the central

cavity, coordinated by four nitrogen atoms, presented in both top and side views of the TM@g-C₁₆N₅ catalyst, alongside a depiction of 27 potential TM atoms on the right. (b) A detailed account of the distal, alternating, consecutive, and enzymatic mechanisms underlying NRR on TM@g-C₁₆N₅. (c) A conceptual "Five-Step" strategy proposed for the efficient screening of potential NRR catalysts. (d) A comprehensive overview and summary illustrating the stability profiles, including E_b , E_f and ΔE_b , for TM@g-C₁₆N₅. (e) Computed Gibbs free energy for N₂ adsorption on TM@g-C₁₆N₅, comparing end-on and side-on adsorption modes. (f)/(g) The evolution of Gibbs free energy associated with the first hydrogenation step ($*N_2 + H^+ + e^- \rightarrow *NNH$ / $*NN + H^+ + e^- \rightarrow *NNH$) of adsorbed N₂ in end-on/side-on orientation. (h) Gibbs free energy change corresponding to the final deamination step on TM@g-C₁₆N₅ ($*NH_2 + H^+ + e^- \rightarrow *NH_3$). (i) A synopsis of the limiting potential (U_L) and the key potential-determining step for TM@g-C₁₆N₅ catalysts (TM = Ti, V, Mo). (j) Evaluation of NRR selectivity for TM@g-C₁₆N₅, based on a comparative analysis of the limiting potentials for NRR and HER.

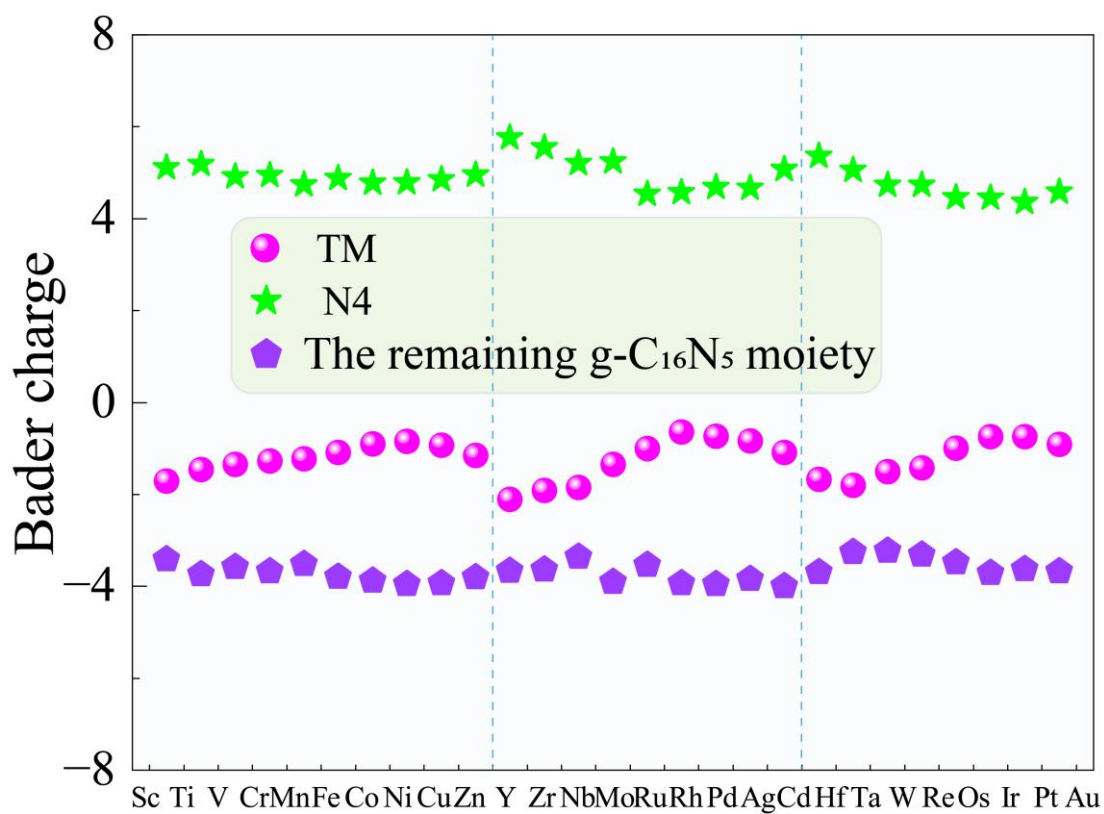


Fig. S2. Bader charge analysis highlighting the charge distribution across different regions of TM@g-C₁₆N₅, where positive values indicate electron acquisition and negative values reflect electron disappearance.

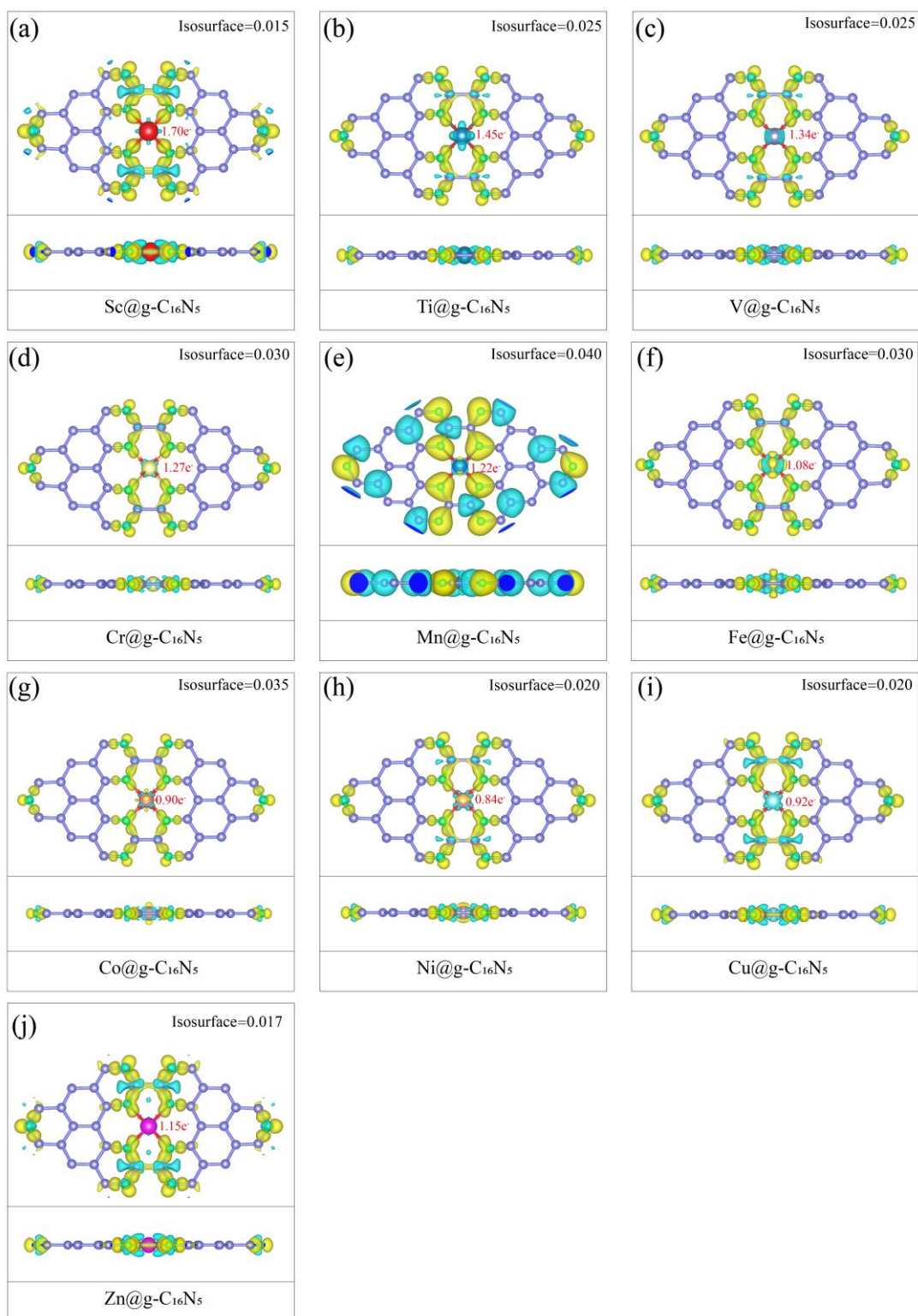


Fig. S3. The differential charge density plots of the TM@g-C₁₅N₆ matrix (from Sc to Zn), with yellow indicating charge accumulation and cyan representing charge depletion, where the top view and side view are given, corresponding values for the isosurfaces are marked in the upper right corner.

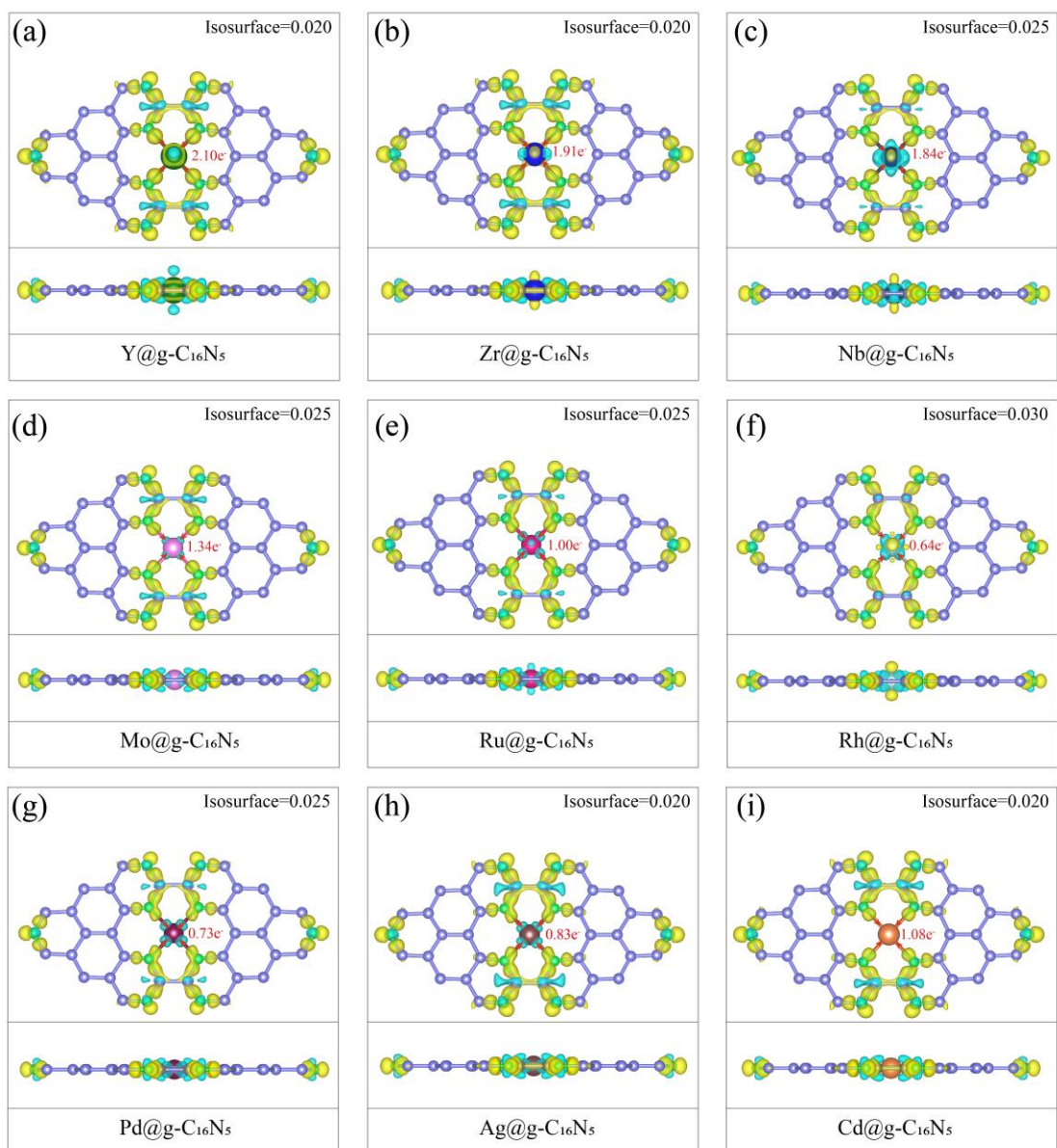


Fig. S4. The differential charge density plots of the TM@-g-C₁₅N₆ matrix (from Y to Cd), with yellow indicating charge accumulation and cyan representing charge depletion, where the top view and side view are given, corresponding values for the isosurfaces are marked in the upper right corner.

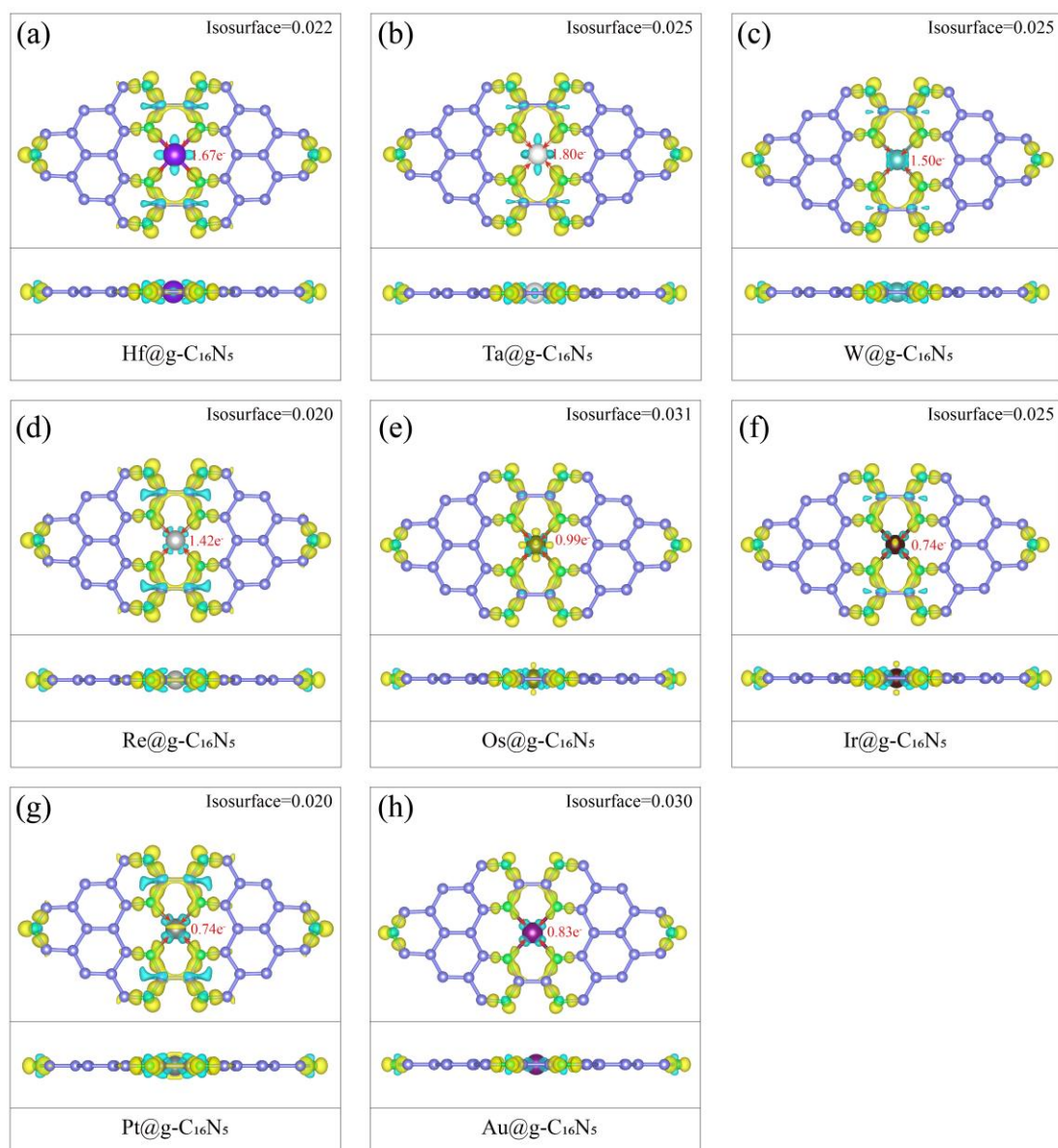


Fig. S5. The differential charge density plots of the TM@g-C₁₅N₆ matrix (from Hf to Au), with yellow indicating charge accumulation and cyan representing charge depletion, where the top view and side view are given, corresponding values for the isosurfaces are marked in the upper right corner.

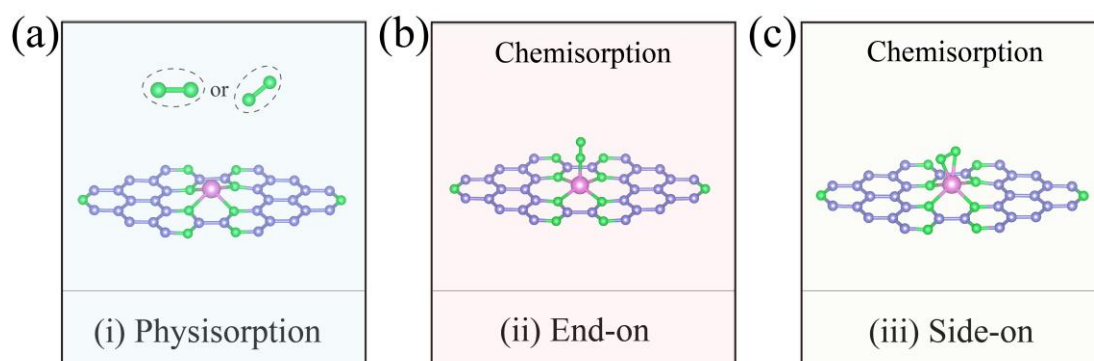


Fig. S6. Three adsorption modes for N_2 molecules on $TM@g-C_{16}N_5$: (a) physisorption; (b) end-on; (c) side-on.

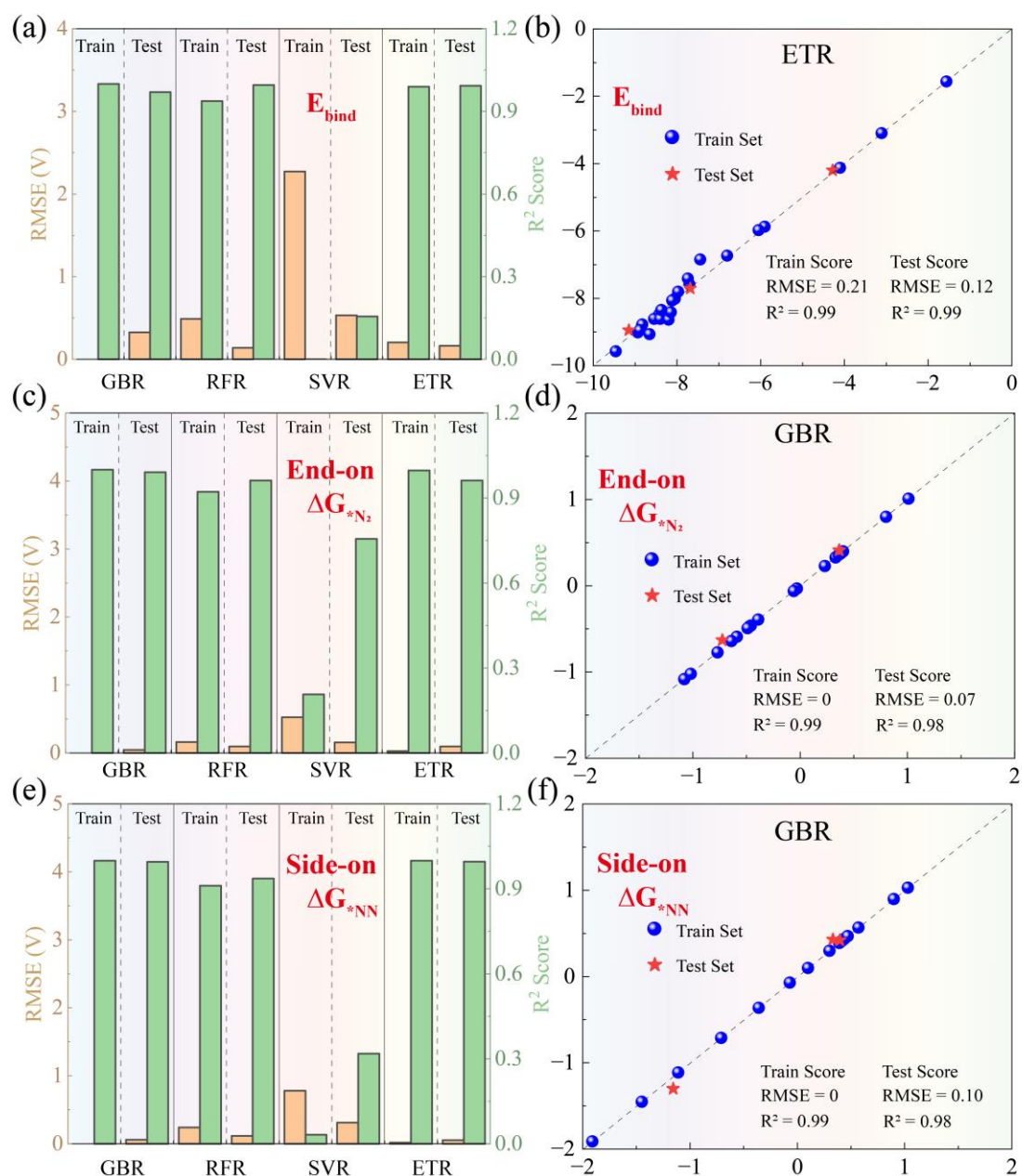


Fig. S7. The left panel denotes the RMSE and R^2 results of the four machine learning algorithms in the training and test sets for binding energy (a), end-on N_2 -adsorption free energy (c), and side-on NN-adsorption free energy (e). For the right panel, a comparison of the DFT calculated and corresponding optimal algorithms shown in the left panel predicted binding energy (b), end-on N_2 -adsorption free energy (d), and side-on NN-adsorption free energy (f).

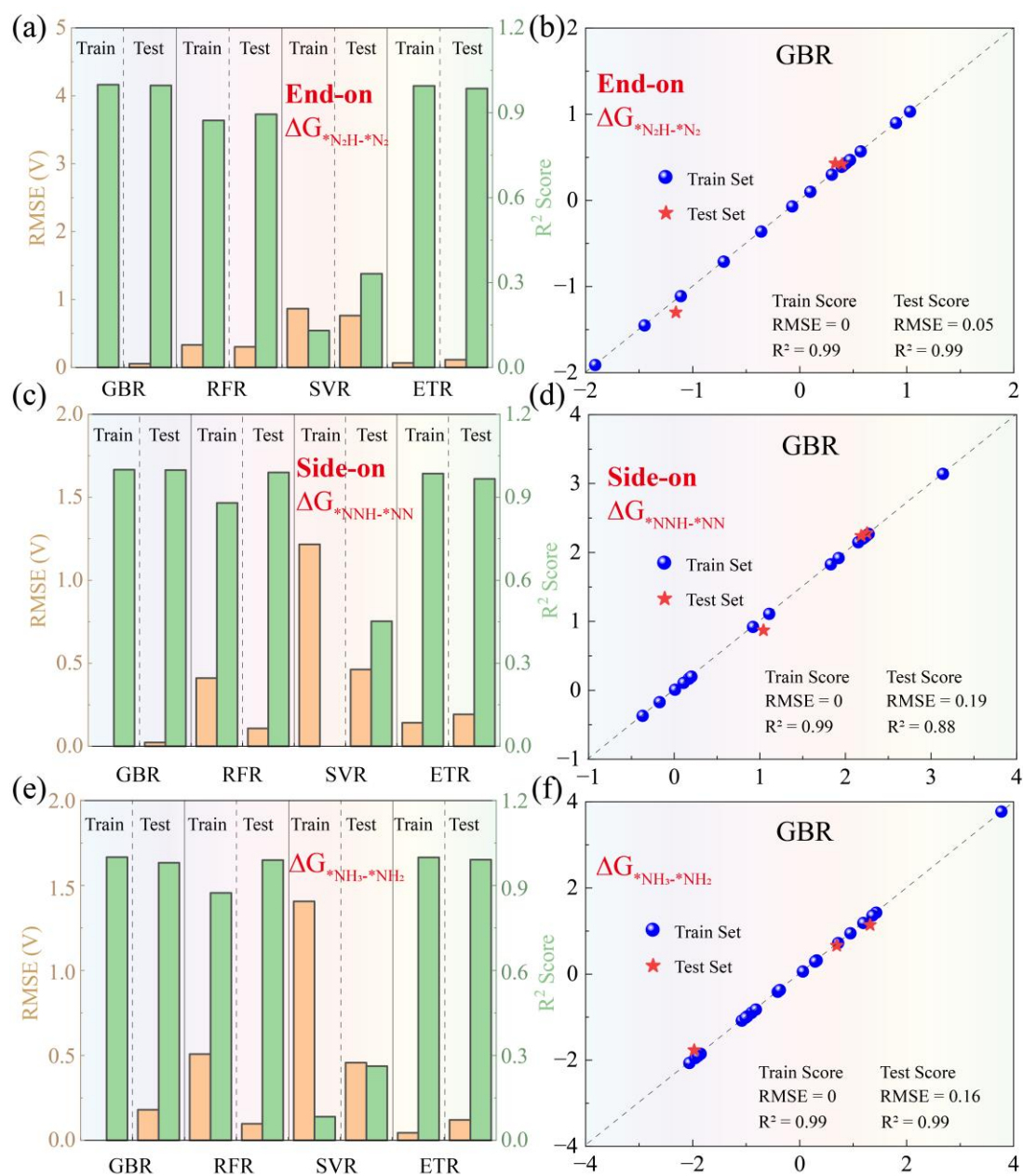


Fig. S8. The left panel denotes the RMSE and R^2 results of the four machine learning algorithms in the training and test sets for the Gibbs free energies of the first end-on step of hydrogenation (a), the first side-on step of hydrogenation (c), and the last step of hydrogenation (e). For the right panel, a comparison of the DFT calculated and corresponding optimal algorithms shown in the left panel predicted the Gibbs free energies of the first end-on step of hydrogenation (b), the first side-on step of hydrogenation (d), and the last step of hydrogenation (f).

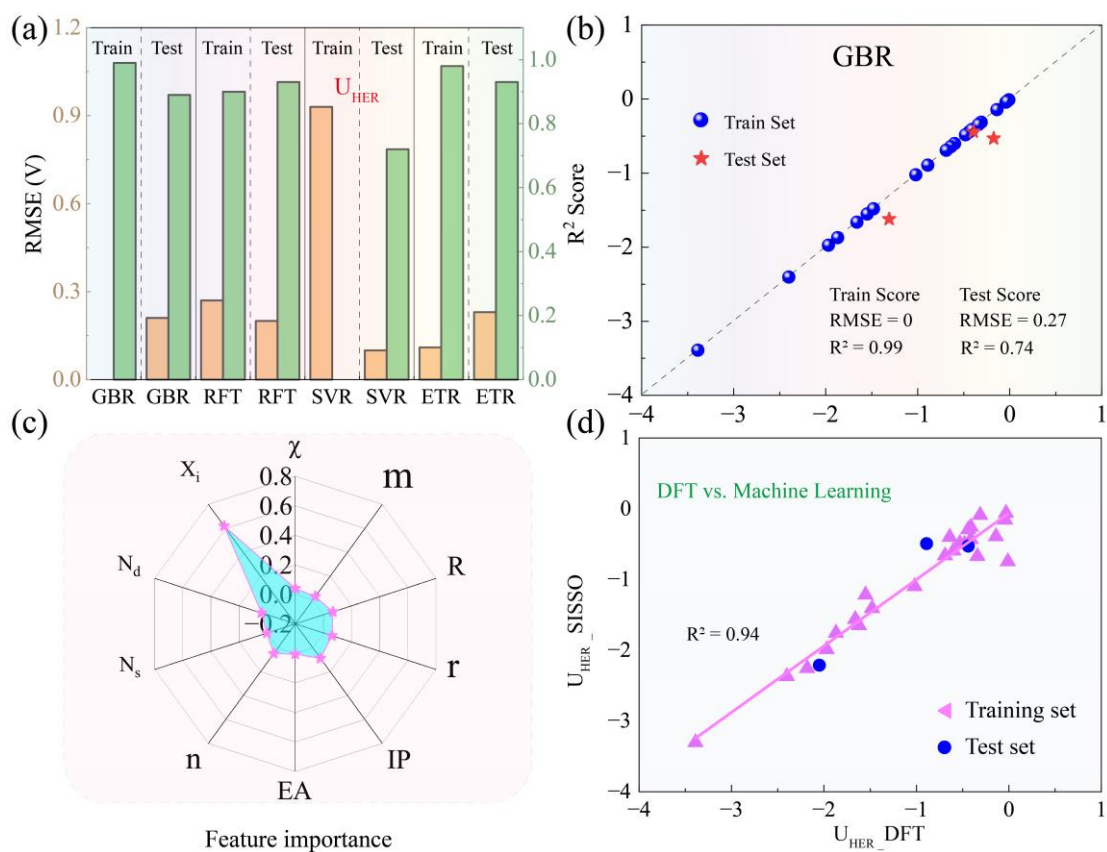


Fig. S9. RMSE and R^2 performance of four ML algorithms on training and test sets in HER (a), alongside a comparison of DFT and GBR-predicted HER overpotentials (b). (c) Predicted feature importance from the GBR algorithm in HER. (d) Comparison between DFT-calculated and SISSO-predicted overpotentials for HER.

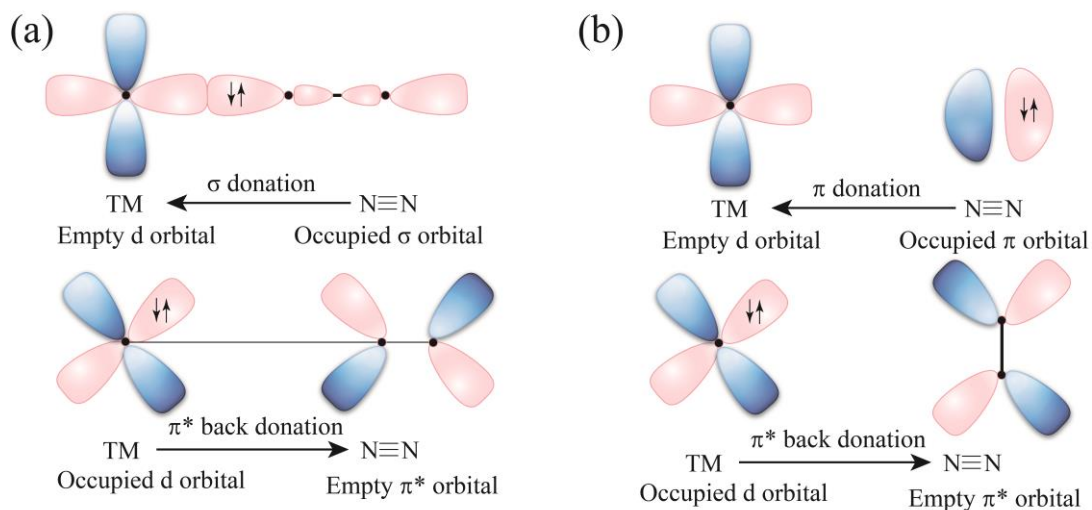


Fig. S10. Schematic representation of N_2 bonding to transition metals, highlighting donation and back-donation in both end-on (a) and side-on (b) orientations.

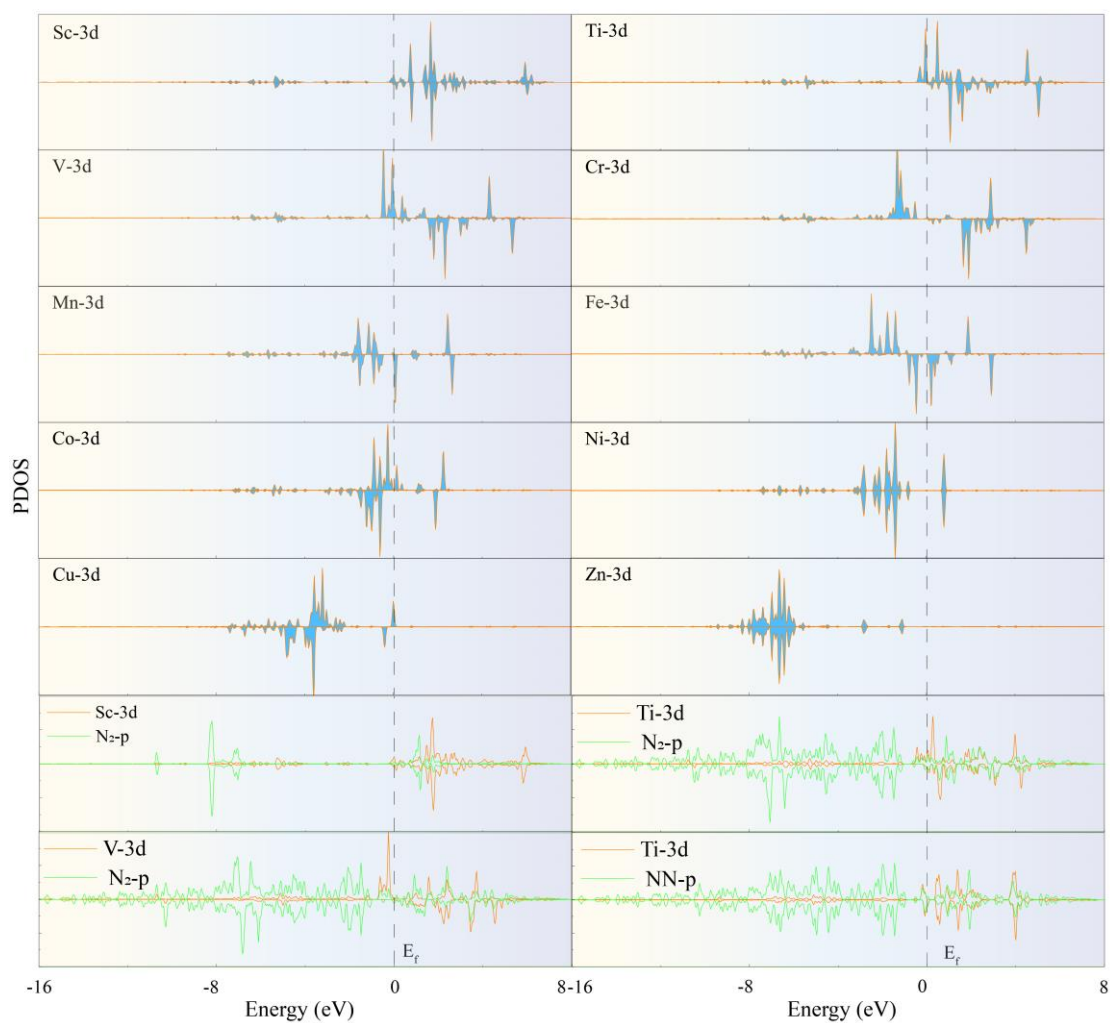


Fig. S11. Partial density of states diagrams for the 3d orbitals of the TM atoms on the TM@g-C₁₆N₅ catalysts prior to or after N₂ adsorption (TM = Sc, Ti, V, Cr, Mn, Fe, Co, Ni, Cu, and Zn).

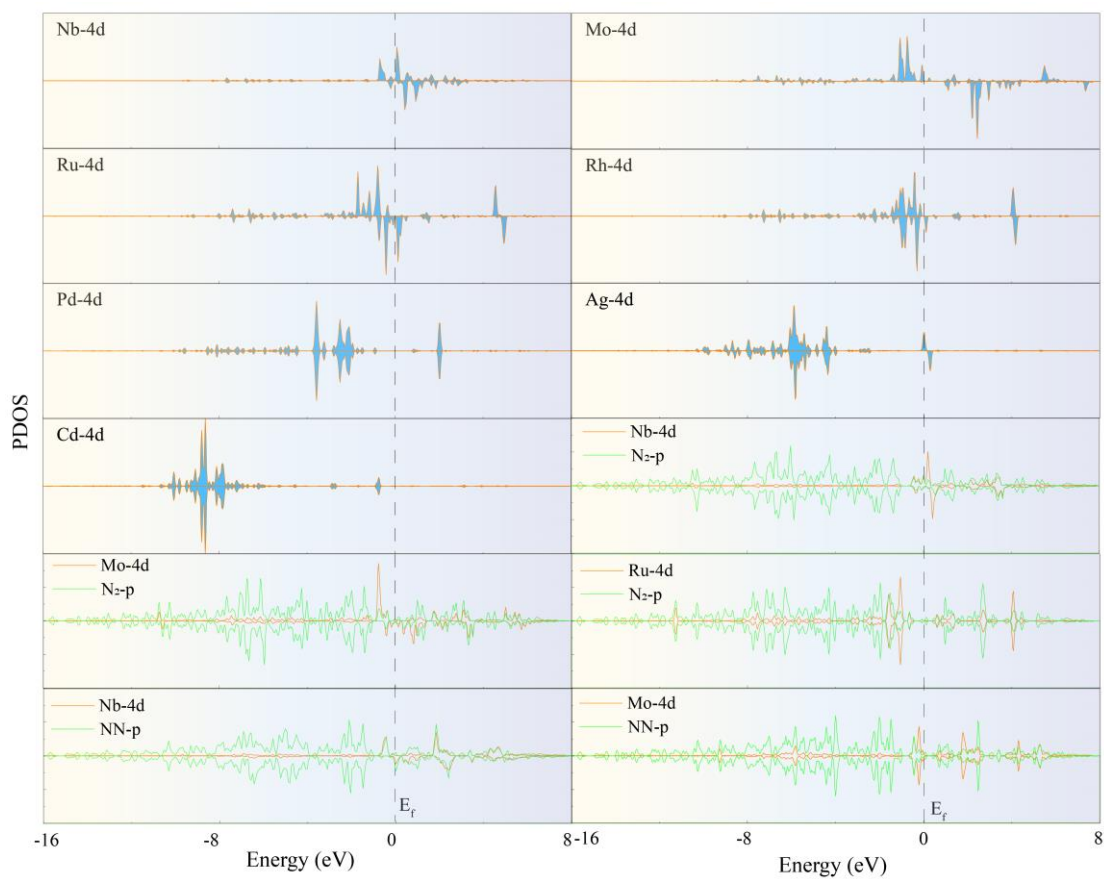


Fig. S12. Partial density of states diagrams for the 4d orbitals of the TM atoms on the TM@g-C₁₆N₅ catalysts prior to or after N₂ adsorption (TM = Nb, Mo, Ru, Rh, Pd, Ag, and Cd).

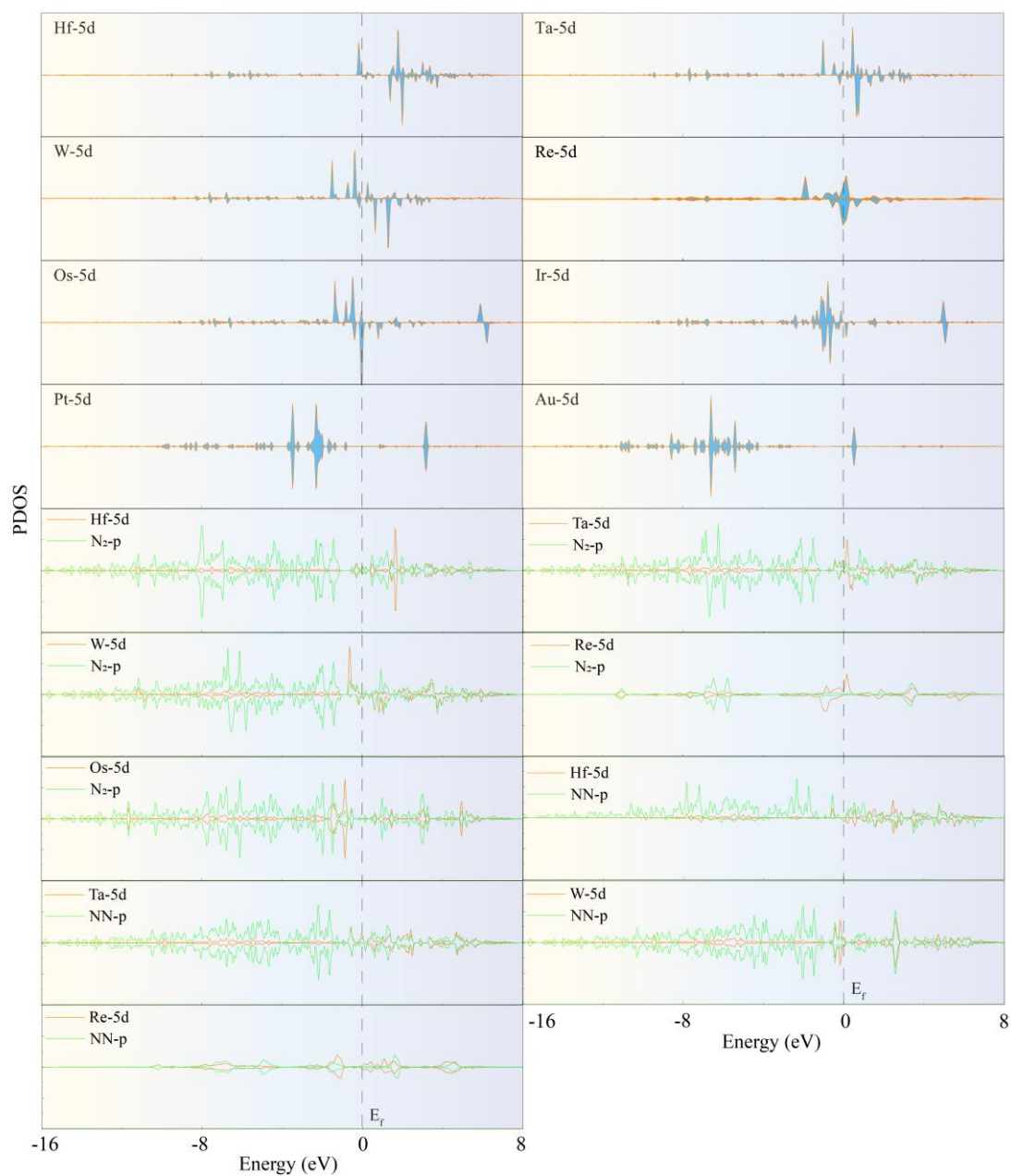


Fig. S13. Partial density of states diagrams for the 5d orbitals of the TM atoms on the TM@g-C₁₆N₅ catalysts prior to or after N₂ adsorption (TM = Hf, Ta, W, Re, Os, Ir, Pt and Au).

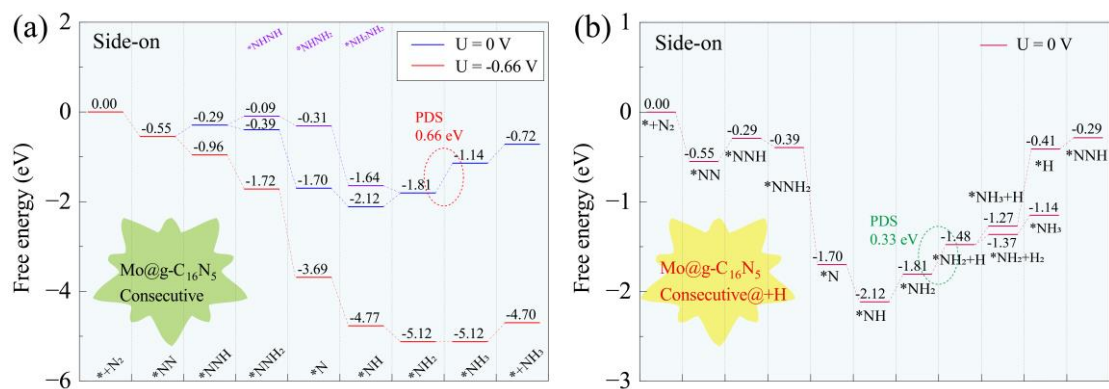


Fig. S14. (a) Reaction energy profile for the consecutive N₂ reduction pathway on Mo@g-C₁₆N₅. (b) Reaction energy profile of the NRR along the consecutive pathway, featuring H⁺ addition to the Mo@g-C₁₆N₅ catalyst when *NH₂ intermediate exists.

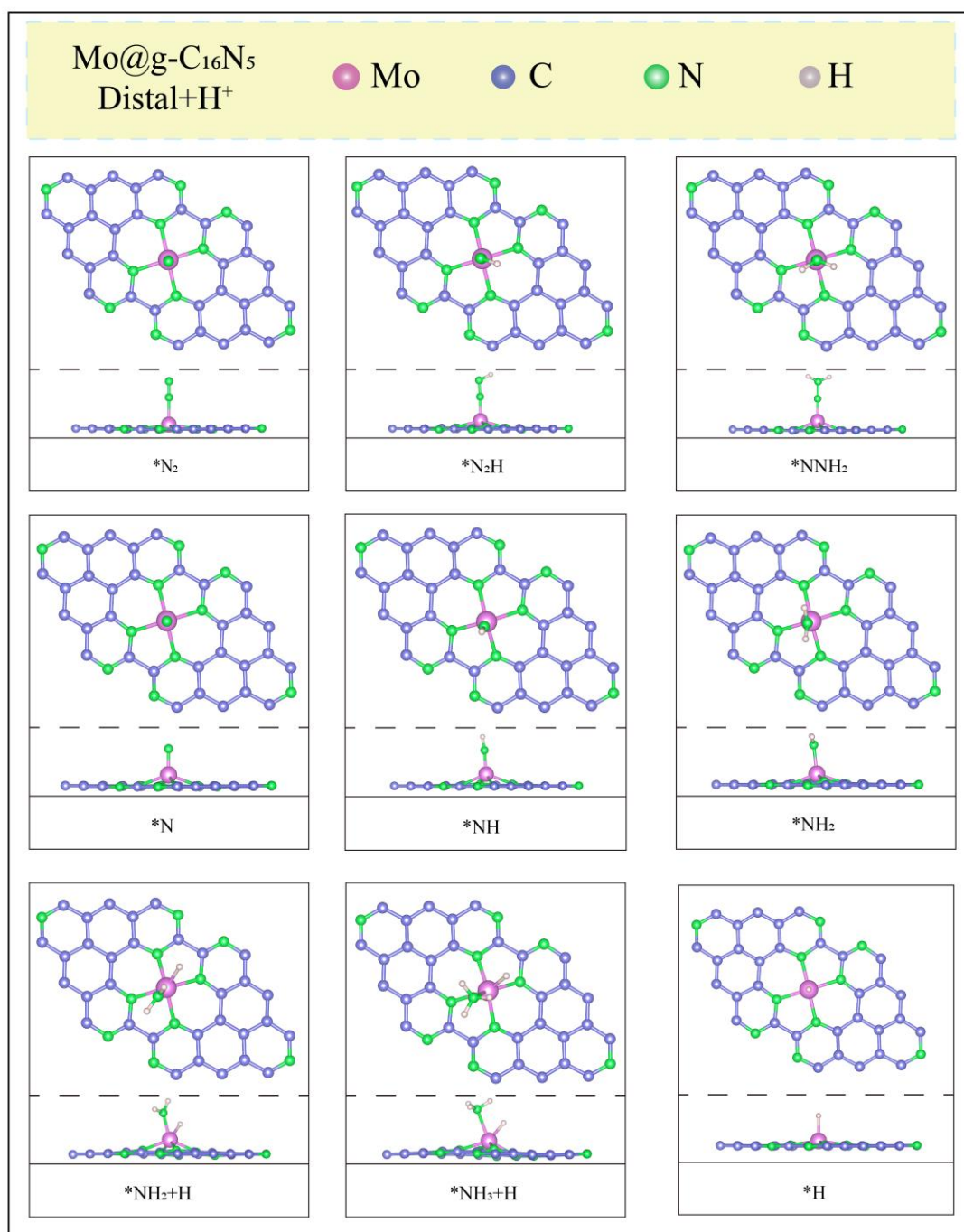


Fig. S15. Structures of key NRR intermediates on $\text{Mo@g-C}_{16}\text{N}_5$ along the most favorable distal pathway, with H^+ added to the Mo atom in the sixth step.

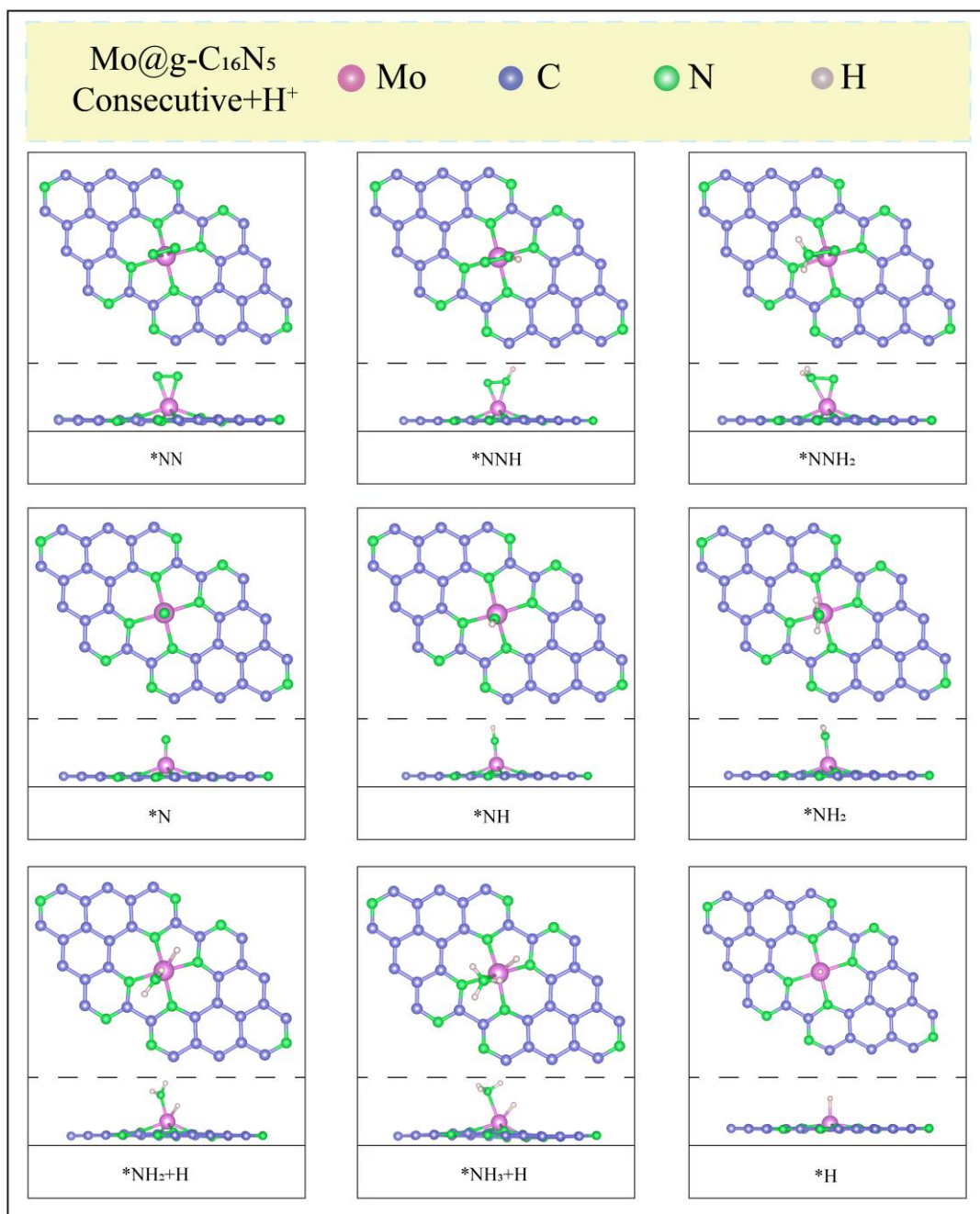


Fig. S16. Structures of key NRR intermediates on $\text{Mo@g-C}_{16}\text{N}_5$ along the most favorable consecutive pathway, with H^+ added to the Mo atom in the sixth step.

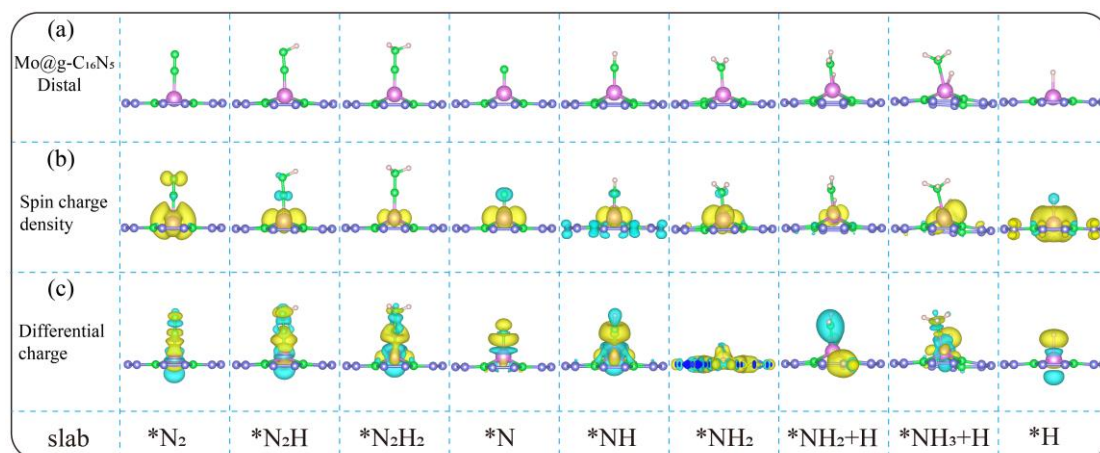


Fig. S17. (a) Structure diagrams of the protonation process of N₂ along the distal pathway, incorporating H⁺ regulation, alongside the corresponding spin density (b) and differential charge density diagrams (c).

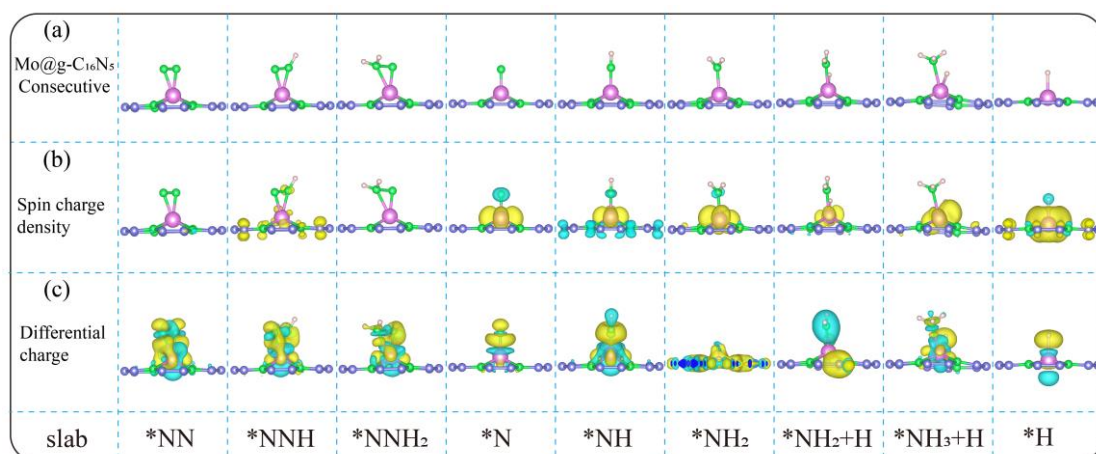


Fig. S18. (a) Structure diagrams of the protonation process of N₂ along the consecutive pathway, incorporating H⁺ regulation, alongside the corresponding spin density (b) and differential charge density diagrams (c).

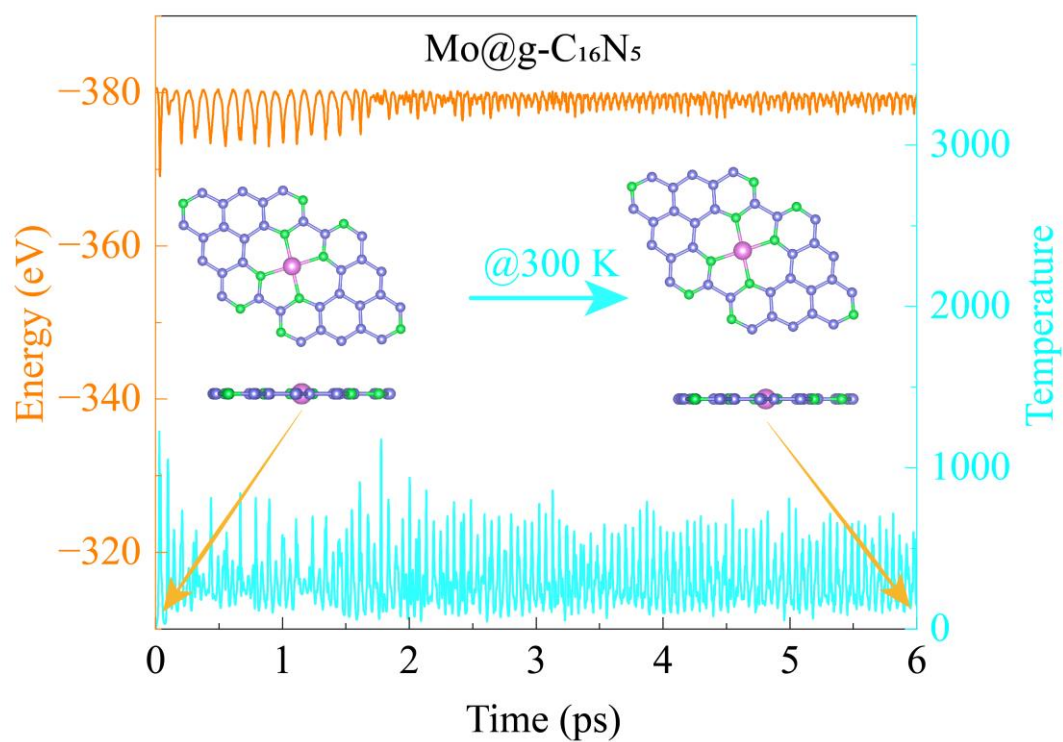


Fig. S19. Variation of total energy and temperature over time during the AIMD simulation at 300 K.

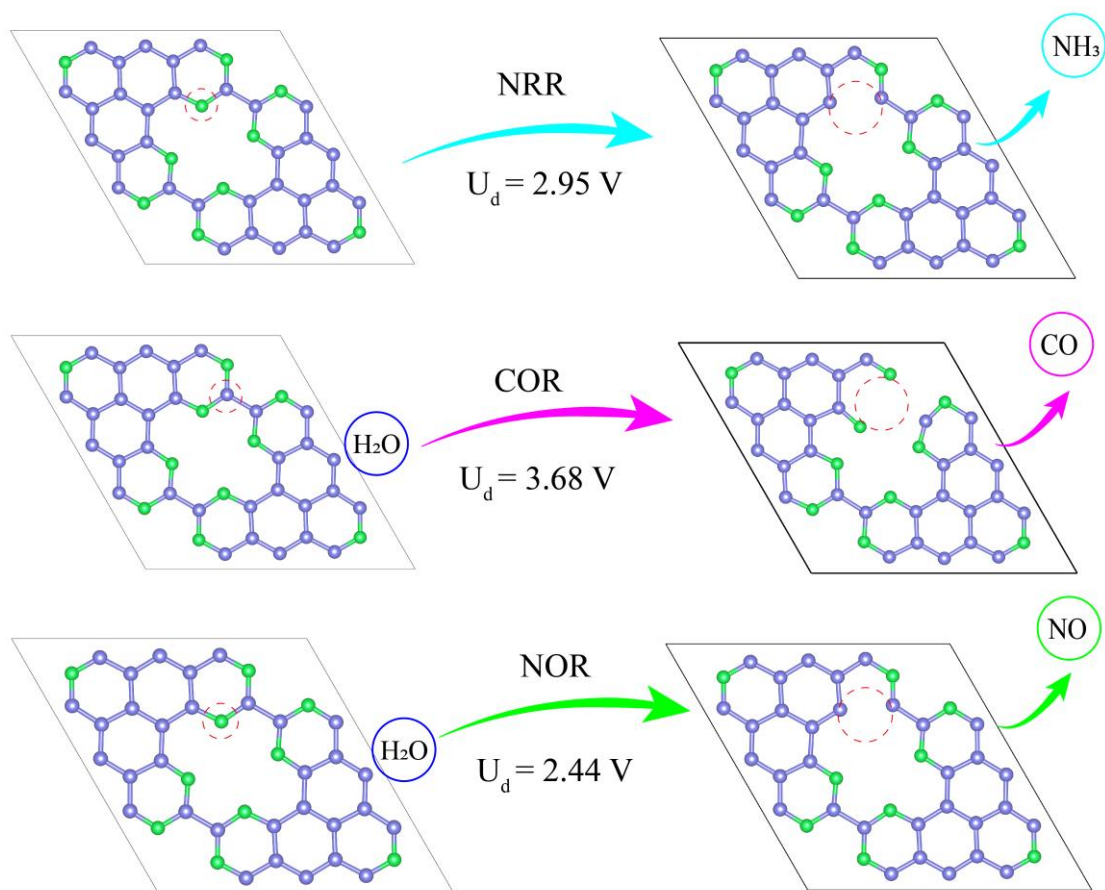


Fig. S20. Dissociation energy required for Mo@g-C₁₆N₅ substrate during NRR, carbon oxidation (COR), and nitrogen oxidation (NOR) reactions.

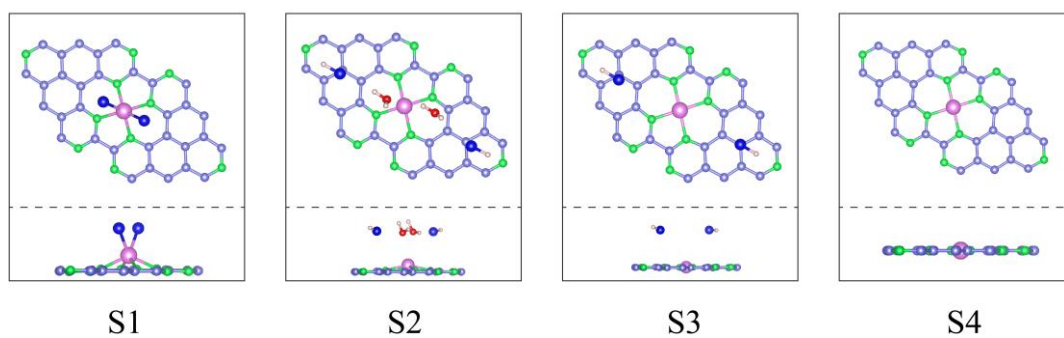


Fig. S21. Schematic of the designed synthetic route for Mo@g-C₁₆N₅, where Cl atoms are represented in navy blue, O atoms are represented in red, H atoms are represented in light pink and other atomic colors as above.

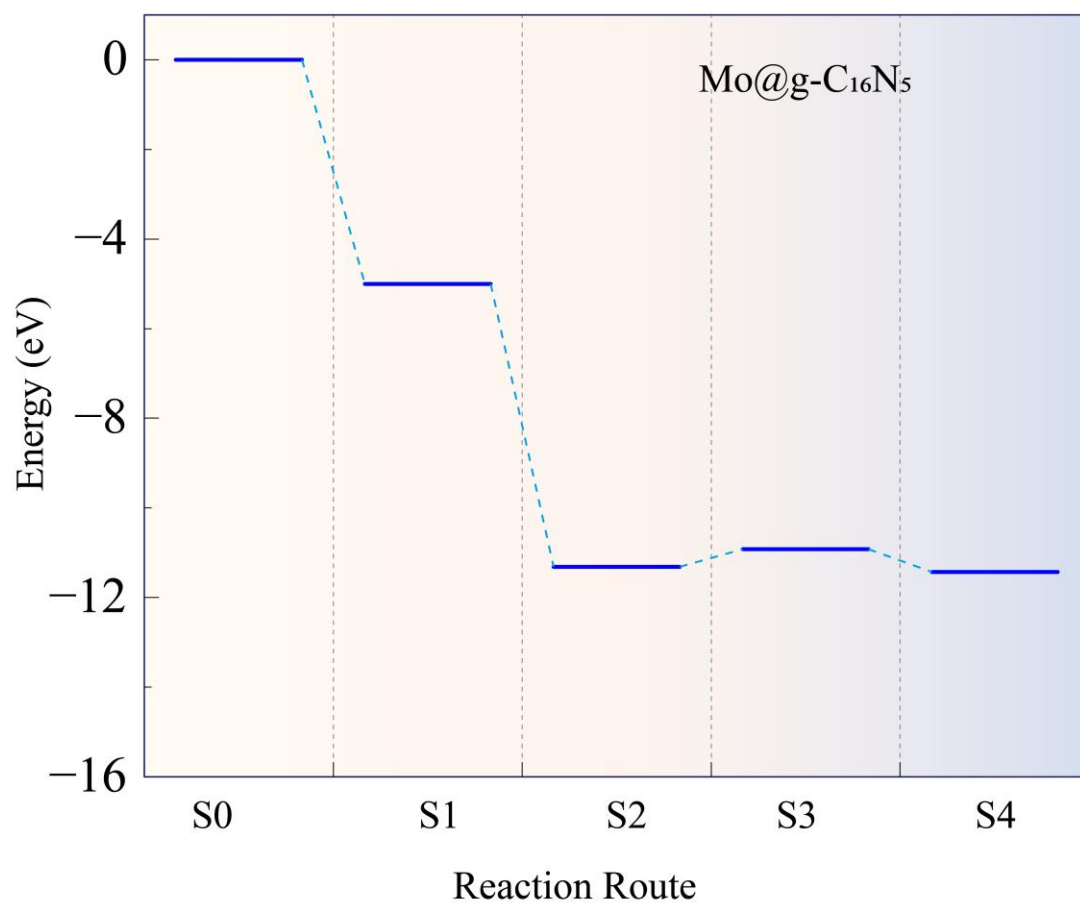


Fig. S22. Energy distribution along the synthetic route depicted in Fig. S21, with S0 representing the initial state of g-C₁₆N₅.

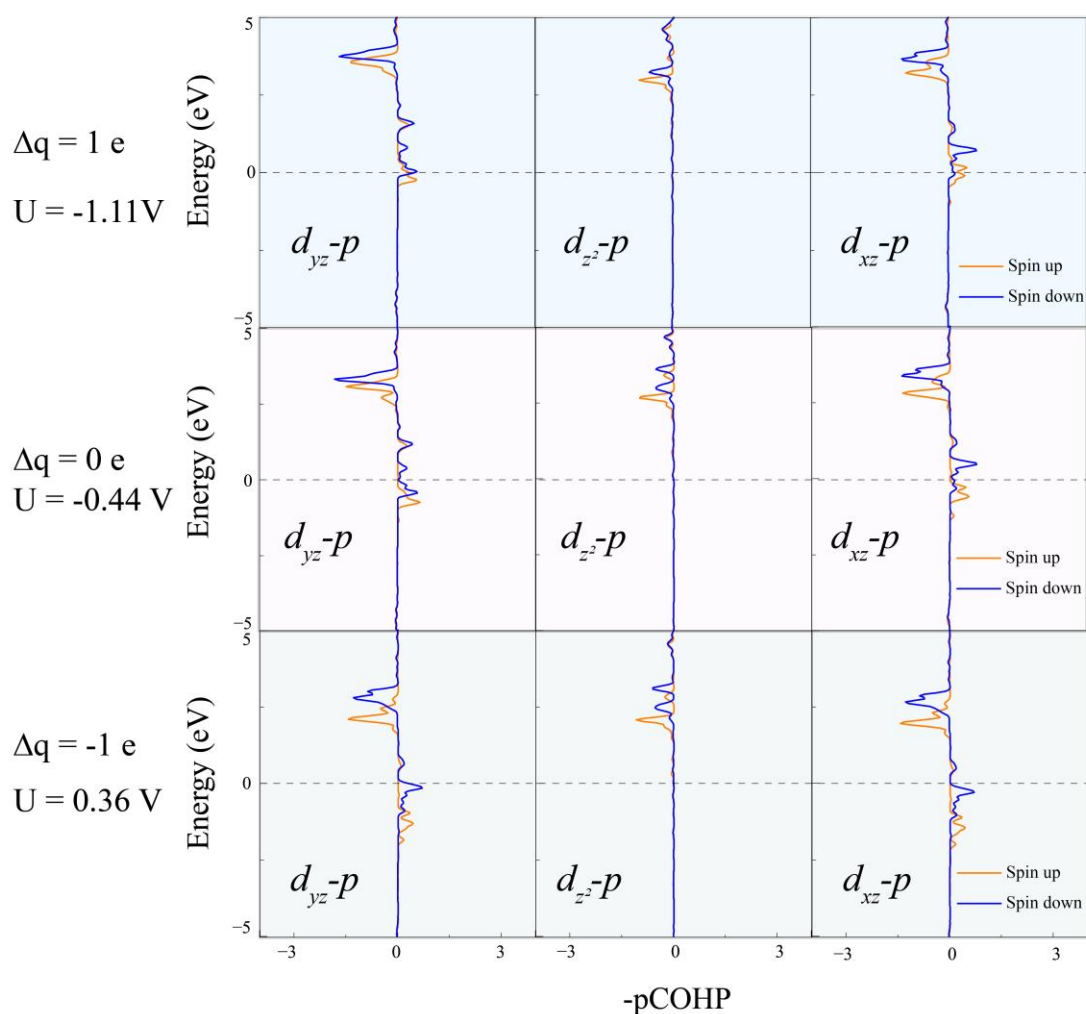


Fig. S23. pCOHP analysis of the Mo-N bond for N₂ adsorption on the Mo@g-C₁₆N₅ catalyst under charge states $\Delta q = +1, 0,$ and $-1 e$, corresponding to electrode potentials of $U = -1.11 V,$ $-0.44 V,$ and $+0.36 V$ vs. SHE, respectively. From left to right, the Figs. illustrate the $-pCOHP$ of the Mo-N bond, followed by the contributions from the Co(d_{yz})-N(p), Co(d_{z^2})-N(p), and Co(d_{xz})-N(p) orbitals, highlighting the orbital interactions that govern the bonding characteristics.

Table S1. Formation energy (E_{form}), binding energy (E_{bind}), cohesive energy (E_{coh}), and energy difference ($\Delta E_b = E_{\text{bind}} - E_{\text{coh}}$) of transition metal atoms anchored on g-C₁₆N₅.

Metals	E_{form} (eV)	E_{bind} (eV)	E_{coh} (eV)	ΔE_b (eV)
Sc	-3.79	-8.01	-4.22	-3.79
Ti	-3.16	-8.63	-5.47	-3.16
V	-3.05	-8.41	-5.37	-3.05
Cr	-3.53	-7.58	-4.05	-3.53
Mn	-3.54	-7.41	-3.87	-3.54
Fe	-3.67	-8.06	-4.39	-3.67
Co	-3.41	-8.61	-5.20	-3.41
Ni	-3.62	-8.47	-4.85	-3.62
Cu	-2.48	-5.97	-3.49	-2.48
Zn	-3.13	-4.20	-1.07	-3.13
Y	-1.69	-5.87	-4.19	-1.69
Zr	-1.50	-7.80	-6.30	-1.50
Nb	-0.72	-7.71	-6.99	-0.72
Mo	-0.48	-6.84	-6.36	-0.48
Ru	-1.44	-9.06	-7.63	-1.44
Rh	-2.73	-8.61	-5.88	-2.73
Pd	-2.99	-6.73	-3.75	-2.99
Ag	-0.57	-3.09	-2.52	-0.57
Cd	-0.82	-1.56	-0.73	-0.82
Hf	-1.85	-8.34	-6.49	-1.85
Ta	-0.75	-8.94	-8.19	-0.75
W	0.13	-8.77	-8.90	0.13
Re	0.03	-9.01	-9.04	0.03
Os	-0.60	-8.95	-8.35	-0.60
Ir	-2.31	-9.57	-7.27	-2.31
Pt	-3.19	-8.79	-5.60	-3.19
Au	-1.08	-4.12	-3.04	-1.08

Table S2. The adsorption free energies of N₂ molecules on the surface of TM atoms in both end-on (left) and side-on (right) attachment modes, along with the TM-N and N-N bond lengths following N₂ adsorption, are summarized, where the symbol “/” denotes an unstable structure that fails to form a stable adsorption configuration.

end-on				side-on			
Atom	ΔE_{*N_2} (eV)	TM-N (Å)	N-N (Å)	ΔE_{*N_2} (eV)	TM-N (Å)	TM-N (Å)	N-N (Å)
Sc	-0.06	2.41	1.12	0.30	3.11	3.42	1.12
Ti	-0.77	2.02	1.14	-0.71	2.11	2.11	1.18
V	-0.49	1.93	1.14	0.10	2.20	2.18	1.15
Cr	0.38	2.46	1.12	0.90	2.11	2.12	1.16
Mn	0.33	2.16	1.12	0.42	2.96	2.95	1.12
Fe	0.23	1.97	1.13	1.03	2.08	2.09	1.15
Co	0.40	1.91	1.12	0.39	3.11	3.42	1.11
Ni	0.37	2.93	1.11	0.42	3.25	3.20	1.11
Cu	0.37	2.87	1.11	0.40	3.26	3.23	1.11
Zn	0.40	3.00	1.11	0.43	3.25	3.22	1.11
Y	\	\	\	\	\	\	\
Zr	\	\	\	\	\	\	\
Nb	-0.63	1.98	1.15	-1.45	2.12	2.11	1.21
Mo	-0.64	1.94	1.15	-0.71	1.98	1.98	1.25
Ru	-0.47	1.83	1.14	0.47	2.13	2.13	1.16

Rh	0.80	2.13	1.12	0.47	3.33	3.34	1.11
Pd	0.38	3.11	1.11	0.43	3.37	3.43	1.11
Ag	0.41	3.06	1.11	0.47	3.41	3.29	1.11
Cd	-0.03	3.44	1.11	-0.07	3.70	3.76	1.11
Hf	-0.39	2.12	1.13	-1.91	2.23	2.23	1.19
Ta	-1.08	2.00	1.15	-1.30	2.10	2.13	1.22
W	-1.02	1.93	1.16	-1.11	1.94	1.94	1.29
Re	-0.59	1.87	1.15	-0.36	1.97	1.97	1.25
Os	-0.46	1.84	1.15	0.57	2.10	2.10	1.18
Ir	1.01	2.06	1.13	0.40	3.35	3.73	1.11
Pt	0.41	3.18	1.11	0.41	3.30	3.62	1.11
Au	0.36	3.22	1.11	0.44	3.35	3.38	1.11

Table S3. The eigenvalues attached to the atomic properties, including the electronegativity (χ), atomic mass (m), atomic radius (R, in pm), ionic radius (r, in pm), the first ionization energy (IP, in kJ/mol), first electron affinity (E_a , in kJ/mol), atomic number (n), s-electron count (N_s), d-electron count (N_d) and outermost electron number (X_i).

materials	χ	m	R	r	IP	EA	n	N_s	N_d	X_i
Sc	1.36	44.96	162	162	633.09	18.14	21	2	1	3
Ti	1.54	47.87	147	86	658.81	7.62	22	2	2	4
V	1.63	50.94	134	79	650.91	50.66	23	2	3	5
Cr	1.66	52.00	128	81	652.87	64.26	24	1	5	6
Mn	1.55	54.94	127	66	717.27	-50.00	25	2	5	7
Fe	1.83	55.85	126	63	762.47	14.57	26	2	6	8
Co	1.88	58.93	125	38	760.40	63.87	27	2	7	9
Ni	1.91	58.69	124	55	737.14	111.54	28	2	8	10
Cu	1.90	63.55	128	60	745.48	119.16	29	1	10	11
Zn	1.65	65.38	134	60	906.40	-58.00	30	2	10	12
Y	1.22	88.91	180	90	599.88	29.62	39	2	1	3
Zr	1.33	91.22	160	59	640.07	41.10	40	2	2	4
Nb	1.60	92.91	146	72	652.13	88.38	41	1	4	5
Mo	2.16	95.95	139	69	684.31	72.17	42	1	5	6
Ru	2.20	101.07	134	68	710.18	101.31	44	1	7	8
Rh	2.28	102.91	134	67	719.67	109.70	45	1	8	9
Pd	2.20	106.42	137	64	804.39	54.23	46	0	10	10
Ag	1.93	107.87	144	100	730.99	125.62	47	1	10	11
Cd	1.69	112.41	149	78	867.77	-68.00	48	2	10	12
Hf	1.30	178.49	159	58	658.52	1.35	72	2	2	4
Ta	1.50	180.95	146	72	728.42	31.07	73	2	3	5
W	2.36	183.84	139	66	758.76	78.76	74	2	4	6
Re	1.90	186.21	137	63	755.82	14.47	75	2	5	7
Os	2.20	190.23	135	63	814.16	106.13	76	2	6	8
Ir	2.20	192.22	136	68	865.18	150.88	77	2	7	9
Pt	2.28	195.08	139	80	864.39	205.32	78	1	9	10
Au	2.54	196.97	144	137	890.12	222.75	79	1	10	11

Table S4. A set of five descriptors, generated by SISO, was designed to quantitatively

describe the energy values.

Target values	Descriptors
E_{*N_2}	$\varphi_{E_{*N_2}} = 115.63 \times \frac{N_d}{R} + 7.2 \frac{(EA \cdot N_s)^3}{R \cdot X_i} \times 10^{-5} - 2.9 \frac{m}{X_i} \cdot \ln EA^2 \times 10^{-3} - 4.3 \chi \cdot X_i \cdot r \cdot N_s^3 \times 10^{-5} - 0.59 \times \frac{\chi}{\ln \frac{m}{r}} - 1.81$
E_{*NN}	$\varphi_{E_{*NN}} = -52.69 \frac{\sqrt{IP}}{r-2R} - 43.27 \frac{EA \cdot n}{X_i^3} - 0.49 \frac{EA}{\ln \frac{m}{r}} + 0.45 \frac{EA}{\ln \frac{r}{m}} + 1.38 \frac{(EA)^3}{r \cdot EA} \times 10^{-2} - 6.98$
$E_{*N_2H-*N_2}$	$\varphi_{E_{*N_2H-*N_2}} = 1.23 \sqrt{\frac{r \cdot N_d}{n+N_s}} + 3.12 \left(\frac{IP \cdot EA}{r \cdot N_d} \right)^2 \times 10^{-5} - 71.84 \frac{(\ln \chi)^2}{\chi^3} + 4.1 \left(\frac{N_d^3 \cdot \chi}{EA} \right)^3 \times 10^{-5} - 1.06 \times 10^{-3} \frac{(\chi \cdot N_d)^3}{EA} + 1.04$
$E_{*NNH-NN}$	$\varphi_{E_{*NNH-NN}} = 1.23 \sqrt{\frac{r \cdot N_d}{n+N_s}} + 3.12 \left(\frac{IP \cdot EA}{r \cdot N_d} \right)^2 \times 10^{-5} - 71.84 \frac{(\ln \chi)^2}{\chi^3} + 4.1 \left(\frac{N_d^3 \cdot \chi}{EA} \right)^3 \times 10^{-5} - 1.06 \times 10^{-3} \frac{EA}{EA} \frac{(\chi \cdot N_d)^3}{N_d} + 1.04$
$E_{*NH_3-*NH_2}$	$\varphi_{E_{*NH_3-*NH_2}} = 3.93 \frac{n}{EA} \times 10^{-4} + 1.34 \frac{n \cdot \ln \chi}{X_i^2} - 4.30 \frac{N_d^3 \cdot \chi \cdot EA}{r} \times 10^{-4} + 82.14 \frac{EA}{(\chi \cdot X_i)^2} + 0.38 \frac{R-r}{(n \cdot N_d)^3} - 1.39$

Table S5. The magnetic moments (in μB) of $\text{TM}@g\text{-C}_{16}\text{N}_5$, examined both before and after N_2 adsorption, are represented using the following notation: "*" for $\text{TM}@g\text{-C}_{16}\text{N}_5$, "* N_2 " for N_2 adsorbed onto TM atoms in an end-on configuration, "* NN " for N_2 adsorbed in a side-on configuration, and "\" to indicate the absence of N_2 adsorption.

materials	*	* N_2	* NN
Sc	0.58	0.51	\
Ti	2.00	1.19	0.12
V	3.01	3.00	\
Cr	3.99	\	\
Mn	0.61	\	\
Fe	1.90	\	\
Co	-0.50	\	\
Ni	0.00	\	\
Cu	-0.91	\	\
Zn	0.00	\	\
Nb	1.37	0.82	1.46
Mo	3.49	1.92	0.00
Ru	1.50	0.00	\
Rh	0.50	\	\
Pd	0.00	\	\
Ag	0.50	\	\
Cd	0.00	\	\
Hf	1.94	0.04	0.50
Ta	1.36	0.93	0.50
W	2.50	2.00	0.01
Re	1.04	-1.00	0.20
Os	1.86	0.00	\
Ir	0.50	\	\
Pt	0.00	\	\
Au	0.00	\	\

Table S6. Quadratic relationship between energy (E) and applied electrochemical potential (U)for bare Mo@g-C₁₆N₅ and NRR intermediates.

Reaction intermediations	Energy (E)	R ²
*	$E = -0.65U^2 - 0.47U - 384.42$	0.998
*N ₂	$E = -0.71U^2 - 0.45U - 402.37$	0.996
*NNH	$E = -0.65U^2 - 0.46U - 405.94$	0.992
*NNH ₂	$E = -0.71U^2 - 0.87U - 410.35$	0.998
*N	$E = -0.52U^2 - 0.10U - 394.60$	0.991
*NH	$E = -0.66U^2 - 0.59U - 398.74$	0.998
*NH ₂	$E = -0.75U^2 - 0.87U - 402.42$	0.998
*NH ₂ +H	$E = -0.65U^2 - 0.62U - 405.53$	0.992
*NH ₃	$E = -0.68U^2 - 1.18U - 406.33$	0.998
*NH ₃ +H	$E = -0.78U^2 - 1.07U - 409.70$	0.990

Table S7. Mo–N bond length (L(Mo–N)), adsorption energy (E_{ads}) across varying U vs SHE potentials for N₂ on Mo@g-C₁₆N₅, and the associated Bader charge (δe) on the adsorbed N₂.

Spin-up and spin-down ICOHP values of the Mo–N bond, with detailed contributions from the five d orbitals (d_{xy} , d_{yz} , d_{z^2} , d_{xz} , and $d_{x^2-y^2}$).

U vs SHE		1.02	0.72	0.46	0.07	-0.46	-0.68	-1.16	-1.43	-1.79
L(Mo-N)		1.99	1.98	1.96	1.95	1.94	1.93	1.91	1.90	1.89
E_{ads}		-1.45	-1.31	-1.33	-1.37	-1.36	-1.43	-1.46	-1.48	-1.58
δe		-0.13	-0.21	-0.28	-0.32	-0.35	-0.44	-0.53	-0.56	-0.60
ICOHP Mo-N	up	-2.95	-2.95	-2.93	-2.91	-2.88	-2.87	-2.84	-2.80	-2.77
total	down	-2.48	-2.51	-2.55	-2.60	-2.62	-2.62	-2.67	-2.73	-2.79
ICOHP										
Mo(d_{xy})-	up	0/0/0	0/0/0	0/0/0	0/0/0	0/0/0	0/0/0	0/0/0	0/0/0	0/0/0
N(p_y)/N(p_z)/N(p_x)	down	0/0/0	0/0/0	0/0/0	0/0/0	0/0/0	0/0/0	0/0/0	0/0/0	0/0/0
ICOHP										
Mo(d_{yz})-	up	-0.43/0/0	0.44/0/0	0.44/0/0	0.44/0/0	0.44/0/0	0.45/0/0	0.44/0/0	0.44/0/0	0.43/0/0
N(p_y)/N(p_z)/N(p_x)	down	0.23/0/0	0.27/0/0	0.31/0/0	0.36/0/0	0.38/0/0	0.39/0/0	0.40/0/0	0.42/0/0	0.44/0/0
ICOHP										
Mo(d_{z^2})-	up	0.55/0	0.54/0	0.52/0	0.51/0	0.50/0	0.48/0	0.47/0	0.46/0	0.45/0
N(p_y)/N(p_z)/N(p_x)	down	0.53/0	0.52/0	0.51/0	0.36/0	0.49/0	0.47/0	0.46/0	0.45/0	0.44/0
ICOHP										
Mo(d_{xz})-	up	0.45	0.47	0.47	0.48	0.48	0.49	0.49	0.49	0.48
N(p_y)/N(p_z)/N(p_x)	down	0.23	0.24	0.25	0.50	0.30	0.31	0.37	0.44	0.50
ICOHP Mo($d_{x^2-y^2}$)-	up	0/0/0	0/0/0	0/0/0	0/0/0	0/0/0	0/0/0	0/0/0	0/0/0	0/0/0
N(p_y)/N(p_z)/N(p_x)	down	0/0/0	0/0/0	0/0/0	0/0/0	0/0/0	0/0/0	0/0/0	0/0/0	0/0/0

Table S8. The E-U relationship for the TM@g-C₁₆N₅ system, fitted using parameters Δq , E_{VASP} , E_f , $E_{\text{Fermi-Shift}}$, U , and potential-dependent electrochemical energy (E), with a fixed Mo-N bond length of 1.64 Å, is expressed as $E = -0.64U^2 - 0.29U - 400.99$.

Δq (e)	E_{VASP} (eV)	E_f (eV)	$E_{\text{Fermi-Shift}}$ (eV)	U (V vs. SHE)	E (eV)
-1.50	-392.93	-5.87	0.40	0.88	-401.74
-1.00	-395.79	-5.53	0.40	0.54	-401.33
-0.50	-398.50	-5.19	0.40	0.19	-401.10
0.00	-400.97	-4.67	0.40	-0.33	-400.97
0.50	-403.22	-4.33	0.40	-0.67	-401.06
1.00	-405.33	-4.02	0.40	-0.97	-401.30
1.50	-407.25	-3.65	0.40	-1.35	-401.79

Table S9. The E-U relationship for the TM@g-C₁₆N₅ system, fitted using parameters Δq , E_{VASP} , E_f , $E_{Fermi-Shift}$, U , and potential-dependent electrochemical energy (E), with a fixed Mo-N bond length of 1.94 Å, is expressed as $E = -0.64U^2 - 0.43U - 402.36$.

Δq (e)	E_{VASP} (eV)	E_f (eV)	$E_{Fermi-Shift}$ (eV)	U (V vs. SHE)	E (eV)
-1.50	-394.42	-5.72	0.40	0.72	-403.00
-1.00	-397.24	-5.46	0.40	0.46	-402.70
-0.50	-399.88	-5.06	0.40	0.06	-402.41
0.00	-402.30	-4.54	0.40	-0.45	-402.30
0.50	-404.50	-4.27	0.40	-0.72	-402.37
1.00	-406.55	-3.84	0.40	-1.15	-402.71
1.50	-408.40	-3.55	0.40	-1.45	-403.08

Table S10. The E-U relationship for the TM@g-C₁₆N₅ system, fitted using parameters Δq , E_{VASP} , E_f , $E_{Fermi-Shift}$, U, and potential-dependent electrochemical energy (E), with a fixed Mo-N bond length of 2.24 Å, is expressed as $E = -0.62U^2 - 0.57U - 401.99$.

Δq (e)	E_{VASP} (eV)	E_f (eV)	$E_{Fermi-Shift}$ (eV)	U (V vs. SHE)	E (eV)
-1.50	-394.17	-5.57	0.40	0.57	-402.52
-1.00	-396.92	-5.36	0.40	0.36	-402.28
-0.50	-399.51	-4.93	0.40	-0.06	-401.98
0.00	-401.86	-4.44	0.40	-0.55	-401.86
0.50	-404.02	-4.17	0.40	-0.82	-401.93
1.00	-405.98	-3.67	0.40	-1.33	-402.32
1.50	-407.76	-3.39	0.40	-1.60	-402.67

Table S11. The E-U relationship for the TM@g-C₁₆N₅ system, fitted using parameters Δq , E_{VASP} , E_f , $E_{Fermi-Shift}$, U, and potential-dependent electrochemical energy (E), with a fixed Mo-N bond length of 2.54 Å, is expressed as $E = -0.79U^2 - 0.71U - 401.36$.

Δq (e)	E_{VASP} (eV)	E_f (eV)	$E_{Fermi-Shift}$ (eV)	U (V vs. SHE)	E (eV)
-1.50	-393.69	-5.48	0.40	0.49	-401.92
-1.00	-396.32	-5.12	0.40	0.12	-401.44
-0.50	-398.84	-4.82	0.40	-0.17	-401.25
0.00	-401.19	-4.59	0.40	-0.41	-401.19
0.50	-403.42	-4.25	0.40	-0.74	-401.29
1.00	-405.46	-3.88	0.40	-1.12	-401.58
1.50	-407.30	-3.47	0.40	-1.53	-402.10

Table S12. The E-U relationship for the TM@g-C₁₆N₅ system, fitted using parameters Δq , E_{VASP} , E_f , $E_{Fermi-Shift}$, U, and potential-dependent electrochemical energy (E), with a fixed Mo-N bond length of 2.84 Å, is expressed as $E = -0.70U^2 - 0.60U - 401.26$.

Δq (e)	E_{VASP} (eV)	E_f (eV)	$E_{Fermi-Shift}$ (eV)	U (V vs. SHE)	E (eV)
-1.50	-393.47	-5.73	0.40	0.74	-402.06
-1.00	-396.22	-5.25	0.40	0.26	-401.48
-0.50	-398.77	-4.89	0.40	-0.10	-401.22
0.00	-401.12	-4.48	0.40	-0.51	-401.12
0.50	-403.32	-4.25	0.40	-0.75	-401.19
1.00	-405.35	-3.81	0.40	-1.18	-401.54
1.50	-407.19	-3.48	0.40	-1.52	-401.97

Table S13. The E-U relationship for the TM@g-C₁₆N₅ system, fitted using parameters Δq , E_{VASP} , E_{F} , $E_{\text{Fermi-Shift}}$, U , and potential-dependent electrochemical energy (E), with a fixed Mo-N bond length of 3.14 Å, is expressed as $E = -0.69U^2 - 0.58U - 401.24$.

Δq (e)	E_{VASP} (eV)	E_{F} (eV)	$E_{\text{Fermi-Shift}}$ (eV)	U (V vs. SHE)	E (eV)
-1.50	-393.44	-5.74	0.40	0.74	-402.04
-1.00	-396.22	-5.30	0.40	0.31	-401.52
-0.50	-398.76	-4.89	0.40	-0.10	-401.20
0.00	-401.11	-4.48	0.40	-0.52	-401.11
0.50	-403.30	-4.25	0.40	-0.75	-401.18
1.00	-405.35	-3.86	0.40	-1.14	-401.49
1.50	-407.17	-3.45	0.40	-1.54	-401.99

Table S14. The E-U relationship for the TM@g-C₁₆N₅ system, fitted using parameters Δq , E_{VASP} , E_f , $E_{Fermi-Shift}$, U , and potential-dependent electrochemical energy (E), with a fixed Mo-N bond length of 3.44 Å, is expressed as $E = -0.70U^2 - 0.58U - 401.23$.

Δq (e)	E_{VASP} (eV)	E_f (eV)	$E_{Fermi-Shift}$ (eV)	U (V vs. SHE)	E (eV)
-1.50	-393.42	-5.73	0.40	0.73	-402.02
-1.00	-396.21	-5.31	0.40	0.32	-401.52
-0.50	-398.74	-4.89	0.40	-0.10	-401.19
0.00	-401.10	-4.48	0.40	-0.51	-401.10
0.50	-403.30	-4.25	0.40	-0.74	-401.17
1.00	-405.35	-3.87	0.40	-1.12	-401.47
1.50	-407.18	-3.45	0.40	-1.55	-402.00

Table S15. The E-U relationship for the TM@g-C₁₆N₅ system, fitted using parameters Δq , E_{VASP} , E_f , $E_{Fermi-Shift}$, U, and potential-dependent electrochemical energy (E), with a fixed Mo-N bond length of 3.74 Å, is expressed as $E = -0.70U^2 - 0.59U - 401.23$.

Δq (e)	E_{VASP} (eV)	E_f (eV)	$E_{Fermi-Shift}$ (eV)	U (V vs. SHE)	E (eV)
-1.50	-393.43	-5.70	0.40	0.71	-401.98
-1.00	-396.20	-5.30	0.40	0.31	-401.51
-0.50	-398.73	-4.89	0.40	-0.11	-401.18
0.00	-401.09	-4.48	0.40	-0.51	-401.09
0.50	-403.29	-4.26	0.40	-0.74	-401.16
1.00	-405.35	-3.89	0.40	-1.11	-401.46
1.50	-407.17	-3.45	0.40	-1.54	-402.00

Table S16. The E-U relationship for the TM@g-C₁₆N₅ system, fitted using parameters Δq , E_{VASP} , E_f , $E_{Fermi-Shift}$, U, and potential-dependent electrochemical energy (E), with a fixed Mo-N bond length of 4.0 Å, is expressed as $E = -0.73U^2 - 0.63U - 401.23$.

Δq (e)	E_{VASP} (eV)	E_f (eV)	$E_{Fermi-Shift}$ (eV)	U (V vs. SHE)	E (eV)
-1.50	-393.48	-5.58	0.40	0.58	-401.85
-1.00	-396.18	-5.33	0.40	0.33	-401.51
-0.50	-398.73	-4.90	0.40	-0.09	-401.18
0.00	-401.09	-4.50	0.40	-0.49	-401.09
0.50	-403.28	-4.25	0.40	-0.74	-401.16
1.00	-405.35	-3.90	0.40	-1.10	-401.45
1.50	-407.17	-3.46	0.40	-1.54	-401.99

References

- 1 J.K. Nørskov, J. Rossmeisl, A. Logadottir, L. Lindqvist, J.R. Kitchin, T. Bligaard, H. Jonsson, *J. Phys. Chem. B*, 2004, **108**, 17886-17892.
- 2 X. Liu, Y. Jiao, Y. Zheng, M. Jaroniec, S.-Z. Qiao, *J. Am. Chem. Soc.*, 2019, **141**, 9664-9672.
- 3 X.-F. Yang, A. Wang, B. Qiao, J. Li, J. Liu, T. Zhang, *Angew. Chem., Int. Edit.*, 2013, **46**, 1740-1748.
- 4 C. Ling, L. Shi, Y. Ouyang, X.C. Zeng, J. Wang, *Nano Lett.*, 2017, **17**, 5133-5139.
- 5 J.H. Friedman, *Comput Stat Data Anal*, 2002, **38**, 367-378.
- 6 J.H. Friedman, *Ann Stat*, 2001, 1189-1232.
- 7 M. Ghobrial, B. Bawamia, T. Cartlidge, I. Purcell, A. Bagnall, M. Farag, M. Alkhalil, *Int J Cardiol*, 2024, **408**, 132159.
- 8 G. Skoufis, *SSRN*, 2024, 11.
- 9 A. Seko, T. Maekawa, K. Tsuda, I. Tanaka, *Phys. Rev. B*, 2014, **89**, 054303.
- 10 T. Peters, B. Molaei, S.R. Evett, G. Merek, *SSRN* 2023, **4500529**,
- 11 R. Ouyang, S. Curtarolo, E. Ahmetcik, M. Scheffler, L.M. Ghiringhelli, *Phys. Rev. Mater.*, 2018, **2**, 083802.
- 12 T.A. Purcell, M. Scheffler, L.M. Ghiringhelli, *J. Chem. Phys.*, 2023, **159**,
- 13 L. Li, X. Wang, H. Guo, G. Yao, H. Yu, Z. Tian, B. Li, L. Chen, *Small Methods*, 2019, **3**, 1900337.
- 14 Q. Zhang, X. Wang, F. Zhang, C. Fang, D. Liu, Q. Zhou, *ACS Appl. Mater. Inter.*, 2023, **15**, 11812-11826.
- 15 Y. Lu, C. Fang, Q. Zhang, Z. Hu, Y. Wu, C. Shi, J. Xu, Y. Li, *J. Power Sources*, 2024, **595**, 234030.
- 16 X. Zhao, G. Hu, G.F. Chen, H. Zhang, S. Zhang, H. Wang, *Adv. Mater.*, 2021, **33**, 2007650.